Report R82-920009-F

COMPUTATION OF LAMINAR AND TURBULENT FLOW IN 90-DEGREE SQUARE-DUCT AND PIPE BENDS USING THE NAVIER-STOKES EQUATIONS

W. R. Briley, R. C. Buggeln and H. McDonald
Scientific Research Associates, Inc.
P.O. Box 498
Glastonbury, CT 06033

April 1982

Final Report for Period 1 March 1981 - 28 February 1982

Prepared for:

OFFICE OF NAVAL RESEARCH
800 N. Quincy Street
Arlington, VA 22217

length scale. Six different flow cases are considered, [illegible] ing flow structure and its dependence on geometric and flow parame[illegible] [illegible]ned. The computed results are compared with available experimental [illegible]lts, and the sequence of comparisons helps to establish the accuracy [illegible]ch these flows can be predicted by the present method using m[illegible]se grids (≈ 10,000 points).

TABLE OF CONTENTS

INTRODUCTION

The flow around bends of various cross section and through other curved flow passages is of considerable importance in internal flow applications. A very common example is that of flow through an elbow or other section of curved pipe connecting two sections of straight pipe. Other examples include that of flow in curved ducts of rectangular or other cross section and flow in more general smoothly-curved passages. Although such geometries are unavoidable in many instances to achieve compact and/or lightweight designs, they are sources of complex secondary flows, losses, and variable heat transfer rates which may affect overall performance or present other design constraints. In other instances, the presence of geometries which produce high total pressure losses or heat transfer may be quite intentional, but accompanied by a need for detailed understanding and/or predictive techniques.

The underlying physical mechanisms present in flows of this type are clearly elucidated by secondary flow theory (reviewed for example by Hawthorne [1,2] and Horlock & Lakshminarayana [3]). In its simplest form, the secondary flow is generated by turning a primary flow in which viscous or other forces upstream have produced a non-zero velocity gradient normal to the plane of curvature. Fluid with above (/below) average momentum migrates to the outside (/inside) of the bend as a result of the radial pressure gradients produced by turning the flow. This phenomenon is quantified by secondary flow theory as the generation of streamwise vorticity from transverse vorticity which has been produced upstream. The secondary velocities are usually quite large (a substantial fraction of the primary velocity) and are influenced by several factors such as flow deflection, strength of inlet vorticity, and thickness of shear regions.

Although the secondary flow is generated by an inviscid mechanism, its strength and subsequent development are influenced in varying degrees by viscous effects. Furthermore, since strong deflections may occur over a short distance, such flows are usually of a transition type and never become fully developed or assume any convenient similarity form. By analogy with external flows, the flow often behaves an an inviscid flow in a central core region, with viscous effects limited to regions near solid boundaries. Unlike most external flow problems, however, the inviscid core region is often not an irrotational potential flow but is rotational with a complex interaction occurring between the two flow regions. Furthermore, as the flow passes through successive flow passages, new viscous and thermal boundary layers develop beneath previous boundary layers, and the distinction between rotational inviscid and viscous boundary layer regions becomes tenuous.

Previous Work

A number of previous investigations have computed flow through strongly curved ducts using approximate forms of the governing equations.

Pratap and Spalding [4] have considered turbulent flow in a strongly curved duct using their "partially parabolic" calculation procedure and a two-equation/wall-function turbulence model. Ghia and Sokhey [5] have computed laminar flow in ducts of strong curvature using a parabolized form of the Navier-Stokes equations. Kreskovsky, Briley and McDonald [6] have recently employed an approximate initial-value analysis for viscous primary and secondary flows to compute laminar and turbulent flow in strongly curved ducts, using a one-equation turbulence model with viscous sublayer resolution. Humphrey, Taylor and Whitelaw [7,8] have obtained laser-Doppler anemometry measurements of laminar and turbulent flow in a square duct of strong curvature, and also performed numerical calculations using a version of the fully-elliptic calculation procedure developed at Imperial College by Gosman, Pun, Patankar and Spalding. Further extensive calculations including heat transfer effects have been made recently by Yee and Humphrey [9].

In view of the general complexity of flow in curved ducts and pipes, including the likely occurrence of flow separation, analysis by numerical solution of the Navier-Stokes equations is both attractive and viable provided efficient numerical methods are used. This approach was recently employed by the authors [10,11] to study laminar and turbulent flow in curved ducts, pipes, and two-dimensional channels. This study concentrated on the square-duct geometry and flow conditions for which detailed measurements have been obtained by Taylor, Whitelaw and Yianneskis [12]. In this study, mesh resolution tests and validation of inflow/outflow boundary conditions were performed on the two-dimensional channel problem. Solutions for laminar and turbulent flow on corresponding square ducts having the same curvature as the channels were computed and compared with measurements from [12]. Good qualitative and reasonable quantitative agreement between solution and experiment was obtained.

In the present investigation, further extensive calculations were performed using the same computational method as in [10,11]. Six flow cases including both laminar and turbulent flow in curved pipes and square ducts are evaluated and compared with available experimental measurements. The laminar square duct of curvature ratio 2.3 (radius of curvature R to hydraulic diameter d) considered in [10,11] was recomputed to test its sensitivity to the grid distribution and other solution parameters. Two turbulent calculations for this same geometry, but having different inlet boundary layer thicknesses are evaluated. One of these cases has a fully-developed inflow and was

chosen because it is one of the evaluation cases for the 1980-81 Stanford Conference on Complex Turbulent Flows for comparison of computation and experiment. Two pipe bends are considered, one laminar and one turbulent, each having a curvature ratio of 2.8. These are compared with the recent measurements of Taylor, Whitelaw and Yianneskis [13]. Finally, turbulent flow in a sharp elbow of curvature ratio 1.0 is considered.

THE PRESENT APPROACH

The present approach is the numerical solution of the compressible Reynolds-averaged Navier-Stokes equations in the low Mach number regime (M = 0.05) for which they approximate the flow of a liquid. The governing equations are solved using an efficient and noniterative time-dependent linearized block implicit (LBI) scheme. With proper treatment of boundary conditions, this algorithm provides rapid convergence which is not significantly degraded by the extreme local mesh resolution which is believed to be necessary for the near-wall sublayer region in turbulent flows. The computational method has been described by the authors in a previous study of flow in duct and pipe bends [10,11]. For completeness, an updated account of the method is included here.

Governing Equations and Coordinate System

The compressible Navier-Stokes equations in general orthogonal coordinates are solved using analytical coordinate data for a system of coordinates aligned with the duct geometry. The compressible time-dependent Navier-Stokes equations are written in orthogonal coordinates in the form given by Hughes and Gaylord [14]. Terms which are identically zero in the coordinate system used are omitted. The first-derivative flux terms are written in conservation form, and for economy the stagnation enthalpy is assumed constant. The definition of stagnation enthalpy and the equation of state for a perfect gas can then be used to eliminate pressure and temperature as dependent variables, and solution of the energy equation is unnecessary. The continuity and three momentum equations are solved with density and the three velocity components aligned with the coordinates as dependent variables.

The coordinate system is shown in Fig. 1 and consists of an axial coordinate x_1 parallel to a curved duct centerline (which lies in the Cartesian x-y plane), and general orthogonal coordinates x_2, x_3 in transverse planes normal to the centerline. Straight extensions are included upstream and downstream of the bend. If the axial coordinate x_1 denotes distance along the centerline and if $K(x_1) \equiv 1/R(x_1)$ is the centerline curvature, then the metric scale factor h_1 for the axial coordinate direction is given by $h_1 = 1 + K(x_1)\,\Delta R(x_2, x_3)$, where $\Delta R \equiv r-R$ is independent of x_1. The transverse metric factors are given by $h_2 = h_3 = 1$ for rectangular (Cartesian) cross sections and by $h_2 = 1$, $h_3 = x_2$ for circular (polar) cross sections. The quantity ΔR is given by $\Delta R = x_3$ and $\Delta R = x_2 \cos x_3$ for Cartesian and polar cross sections, respectively. The centerline curvature K is discontinuous when a straight segment of a duct joins a constant radius segment. To remove the associated coordinate singularity, the flow

geometry is smoothed over an axial distance of o. duct diameter. This is accomplished using a fifth-order polynomial variation in K which matches function value, first and second derivatives of K at the end points of the smoothing region. Analytical coordinate transformations due to Roberts [15] were used to redistribute grid points and thus improve resolution in shear layers. Derivatives of geometric data were determined analytically for use in the difference equations. A nonuniform mesh distribution was employed for the axial coordinate x_1 to concentrate grid points inside the curved section of the duct or pipe. Representative grids for the cross sectional planes are shown in Fig. 2.

Turbulence Model

The turbulence model used falls into the category of one-equation turbulence models discussed by Launder and Spalding [16], and parallels the method given by Shamroth and Gibeling [17]. This model requires solution of a single partial differential equation governing turbulence kinetic energy k, in conjunction with a specified length scale ℓ. A turbulent viscosity μ_t is obtained from the Prandtl-Kolmogorov constitutive relationship $\mu_t \alpha \ell k^{1/2}$. The turbulent viscosity μ_t is assumed to be isotropic, and the stress tensor in the ensemble-averaged equation is determined by adding the turbulent viscosity to the molecular viscosity μ to obtain the total effective viscosity $\mu_e = \mu + \mu_t$. Given an estimate of the length scale at the edge of the viscous layer and its streamwise growth rate, a distribution of mixing length within the viscous layer can be obtained from semi-empirical relationships widely used in two- and three-dimensional boundary layer calculations. To estimate the axial growth rate of the shear layer, a boundary layer momentum integral procedure which neglects axial curvature but includes blockage effects is used. The final turbulence model provides for resolution of the viscous sublayer region near walls.

The equation governing turbulence kinetic energy is given by Launder and Spalding [18] for Cartesian coordinates and is rewritten in the present orthogonal coordinate system. The turbulent viscosity is obtained from the Prandtl-Kolmogorov relation

$$\mu_t = c_\mu \rho k^2/\varepsilon = c_\mu^{1/4} \rho k^{1/2} \ell \tag{1}$$

where the dissipation rate ε is given by

$$\varepsilon = c_\mu^{3/4} k^{3/2}/\ell \tag{2}$$

For high Reynolds number flow, c_μ is approximately 0.09. For low Reynolds number and in the viscous sublayer, c_μ is given a prescribed dependence on turbulence Reynolds number R_τ in the manner suggested by McDonald and Fish [19] for transitional boundary layer flows. In [19], the turbulence Reynolds number R_τ was appropriately defined as an integral average across the boundary layer. Here and following [17], it is convenient to define R_τ as the local ratio of turbulent to laminar viscosity $R_\tau = \mu_t/\mu$. The structural coefficient c_μ is given in [19] as $c_\mu = 4(a_1)^2$, where

$$a_1 = a_o \, f(R_\tau) \; / \; [1 + 6.66 \, a_o(f(R_\tau)-1)] \tag{3}$$

where $a_o = 0.0115$ and

$$f(R_\tau) = \begin{cases} R_\tau^{0.22} & R_\tau \leq 1 \\ 6.81 \, R_\tau + 6.143 & R_\tau \geq 40 \end{cases} \tag{4}$$

with a cubic polynomial curve fit for values of R_τ between 1 and 40.

It remains to specify a length scale distribution appropriate for the problem under consideration. The length scale distribution is adapted from previous turbulence models for turbulent boundary layers and taken to be the conventionally defined mixing length of Prandtl. The distribution of mixing length given by McDonald and Fish [19] has proven effective for a wide range of two-dimensional turbulent boundary layers and is easily adapted for present use. This distribution is given by

$$\ell = \mathcal{D} \, \ell_\infty \tanh \, (\kappa d/\ell_\infty) \tag{5}$$

where ℓ is mixing length, ℓ_∞ is an outer-region value of mixing length, d is distance from the wall, κ is the von Karman constant (taken here as 0.41), and $\mathcal{D}$ is a sublayer damping function given by

$$\mathcal{D} = P^{1/2} \; [(d^+-23)/8] \tag{6}$$

Here, P is the normal probability function and d^+ is defined by $d^+ = d(\tau/\rho)^{1/2}/\nu$, where τ is shear stress and ν is kinematic viscosity. For equilibrium boundary layers, ℓ_∞ is observed to have a constant value of about 0.09 δ, where δ is the local boundary layer thickness.

The length scale distribution of Eq. (5) is adapted for present use by taking d as distance to the nearest wall and by assigning ℓ_∞ a distribution based on two-dimensional momentum integral estimates of the boundary layer growth rates. The computed estimates of boundary layer growth were obtained from a simple integral prediction scheme which neglects axial curvature, rather than an attempt to scan the intermediate transient solutions of the Navier-Stokes equations to determine some ill-defined boundary layer

thickness. Assuming a 1/7 power law velocity profile and a skin friction law $c_f/2 = 0.0225\ (\nu/u_e\delta)^{1/4}$, the momentum integral equation for a two-dimensional straight channel can be written as

$$h_1 \frac{d\delta}{dx} + h_2 \frac{\delta}{u_e} \frac{du_e}{dx} = c_f/2 \qquad (7)$$

where for the 1/7 power profile: $h_1 = 7/72$ and $h_2 = 23/72$. An analogous equation is easily derived for flow in a straight pipe. The free stream velocity is then related to the boundary layer thickness by an ancillary formula which approximates the blockage effects associated with internal flow. This relationship between δ and u_e is inserted into (. .) prior to solution. Eq. (7) is solved using a second-order linearized finite difference scheme described in [23]. The outer or maximum mixing length scale associated with each axial location is determined from the formula $\ell_\infty = 0.09\ \delta$, where δ is the computed value from Eq. (7).

Physical Boundary and Initial Conditions

The computational domain includes the curved portion of the duct or pipe comprising the 90-degree bend and short straight extensions upstream and downstream of the bend. The computational domain is thus embedded within a larger overall flow system and requires inflow and outflow boundary conditions which adequately model the interface between the computed flow and the remainder of the flow system. The inflow/outflow conditions used are derived from an assumed flow structure and are chosen to provide inflow with prescribed stagnation pressure (and stagnation enthalpy) in an inviscid core region and with a given axial velcoity profile shape in the inflow boundary layer, and to provide outflow with a prescribed distribution of static pressure in the cross section. These boundary conditions are compatible both with an inviscid characteristics analysis and with the physical process by which most such flows are established. Physically, a duct flow is often established by supplying air of a given stagnation pressure and temperature and exhausting the duct at a given static pressure. The mass flux through the duct may then vary with time until a steady state is achieved, at which the mass flux is determined as a balance between these inflow/outflow quantities and viscous and thermal effects within the duct. By choosing stagnation pressure and temperature at inflow and static pressure at outflow as the dominant boundary conditions, the present solution procedure allows both velocity and static pressure to vary with time at the inflow boundary, as is consistent with this

physical process. As a consequence, pressure waves are transmitted upstream through the inflow boundary during the transient flow process and are not reflected back into the computational domain. The reflection of pressure waves at an inflow boundary when velocity and pressure are fixed in time has often been cited as a cause of either instability or slow convergence in other investigations. These boundary conditions are discussed in more detail in [20]. The specific treatment of initial and boundary conditions used here is outlined below.

The initial and boundary conditions are devised from estimates of the potential flow velocity $\bar{U}_1(x_1, x_2, x_3)$ for the duct, a mean boundary layer thickness $\delta(x_1)$ for shear layers on transverse duct or pipe walls, and finally from an estimate of the blockage correction factor $B(x_1)$ for the core flow velocity due to the boundary layer growth. The potential flow velocity is approximated as uniform flow in straight segments of the duct and as Cr^{-1} in curved segments. Taking C as $(R_o - R_i)/\ell n(R_o/R_i)$ and $d^2/8[R- (R^2-d^2/4)^{1/2}]$ leads to a unit mass flux for rectangular and circular cross sections, respectively. Here, R_i and R_o are the radii to the inner and outer walls of the duct, $R = (R_i + R_o)/2$, and d is the pipe diameter (cf. Fig. 1). Distributions of $\delta(x_1)$ and $B(x_1)$ are determined by recourse to the simple one-dimensional momentum integral analysis mentioned in describing the turbulence model. Finally, a shear layer velocity profile shape $f(\bar{y}/\delta)$, $o \leq f \leq 1$ is chosen for each problem, where $\bar{y}$ is a parameter indicative of distance from a wall. For laminar flow cases, von Karman polynomial velocity profiles were used. For turbulent flow cases, these velocity profile shapes were taken from the analytical fit of Musker [21] to the Coles type of profile which matches δ^* and c_f from the momentum-integral calculations. The initial values of velocity components u_1, u_2, u_3 are given by

$$U_1 = U_I \, B(x_1) \, f \, [\bar{y}/\delta(x_1)]$$

$$U_2 = U_3 = 0$$

In the pipe flow calculations, estimates of the inflow radial velocity u_2 were available and were used as initial conditions. The details of this procedure are not critical and are omitted, since except for the shape and thickness of the inlet boundary layer profile, these results serve only as a convenient method for selecting initial conditions. A reasonably accurate estimate for the pressure drop which will produce the desired flow rate must be made using any convenient source, such as a Moody diagram, data correlations, momentum integral analysis, or other computed results. A smooth axial distribution of pressure which matches this pressure drop is then assigned and adjusted to approximate local curvature of the flow geometry.

This completes specification of the initial conditions. It is noted that although these initial conditions do take into account several relevant features of the flow, the important effects of strong secondary flows and their distortion of the primary flow are completely neglected. The resulting initial flow is thus a simple but relatively crude approximation to the final flow field.

At the inflow boundary, a "two-layer" boundary condition is devised such that stagnation pressure p_o is fixed in the core flow region and an axial velocity profile shape $u_1/u_e = f(\bar{y}/\delta)$ is set within shear layers. Here, u_e is the local edge velocity which varies with time and is adjusted after each time step to the value consistent with p_o and the local edge static pressure determined as part of the solution. The transverse velocity components u_2 and u_3 were also specified at inflow. For the pipe flow cases, u_3 was set to zero, and the radial velocity u_2 was given a smooth distribution consistent with the boundary layer thickness and estimated axial pressure drop. For the duct flow cases, u_2 and u_3 were extrapolated until the initial impulsive transients had passed and were then held fixed. The remaining inflow condition is $\partial^2 c_p/\partial n^2 = g(x_2, x_3)$, where n denotes the normal coordinate direction and c_p is pressure coefficient referred to reference conditions. The quantity g is computed from the initial conditions with c_p defined as $1-(BU_I)^2$, its value from the potential flow corrected for estimated blockage. For outflow conditions, the static pressure is imposed, and second normal derivatives of each velocity component are set to zero. At no-slip walls, all velocity components are set to zero, and the remaining condition used is $\partial p/\partial n = 0$, where p is pressure. The condition $\partial p/\partial n = 0$ at a no-slip surface approximates the normal momentum equation to order Re^{-1} for viscous flow at high Reynolds number. Finally, the three-dimensional flow cases are assumed to be symmetric about the plane containing the curved duct centerline, and symmetry conditions are imposed on this boundary.

SOLUTION PROCEDURE

Background

The solution procedure employs a consistently-split linearized block implicit (LBI) algorithm which has been discussed in detail by the authors in [22,23]. There are two important elements of this method:

(1) the use of a noniterative formal time linearization to produce a fully-coupled linear multidimensional scheme which is written in "block implicit" form; and

(2) solution of this linearized coupled scheme using a consistent "splitting" (ADI scheme) patterned after the Douglas-Gunn [24] (1964) treatment of scalar ADI schemes.

The method is thus referred to as a split linearized block implicit (LBI) scheme. The method has several attributes:

(1) the noniterative linearization is efficient;

(2) the fully-coupled linearized algorithm eliminates instabilities and/or extremely slow convergence rates often attributed to methods which employ ad hoc decoupling and linearization assumptions to identify nonlinear coefficients which are then treated by lag and update techniques;

(3) the splitting or ADI technique produces an efficient algorithm which is stable for large time steps and also provides a means for convergence acceleration for further efficiency in computing steady solutions;

(4) intermediate steps of the splitting are consistent with the governing equations, and this means that the "physical" boundary conditions can be used for the intermediate solutions. Other splittings which are inconsistent can have severe difficulties in satisfying physical boundary conditions [23].

(5) the convergence rate and overall efficiency of the algorithm are much less sensitive to mesh refinement and redistribution than algorithms based on explicit schemes or which employ ad hoc decoupling and linearization assumptions. This is important for accuracy and for computing turbulent flows with viscous sublayer resolution; and

(6) the method is general and is specifically designed for the complex systems of equations which govern multiscale viscous flow in complicated geometries.

This same algorithm was later considered by Beam and Warming [25], but the ADI splitting was derived by approximate factorization instead of the Douglas-Gunn procedure. They refer to the algorithm as a "delta form" approximate factorization scheme. This scheme replaced an earlier non-delta form scheme [26], which has inconsistent intermediate steps.

Spatial Differencing and Artificial Dissipation

The spatial differencing procedures used are a straightforward adaption of those used in [22] and elsewhere. Three-point central difference formulas are used for spatial derivatives, including the first-derivative convection and pressure gradient terms. This has an advantage over one-sided formulas in flow calculations subject to "two-point" boundary conditions (virtually all viscous or subsonic flows), in that all boundary conditions enter the algorithm implictly. In practical flow calculations, artificial dissipation is usually needed and is added to control high-frequency numerical oscillations which otherwise occur with the central-difference formula.

In the present investigation, artificial (anisotropic) dissipation terms of the form

$$\sum_j \frac{d_j}{h_j^2} \frac{\partial^2 u_k}{\partial x_j^2} \tag{8}$$

are added to the right-hand side of each (k-th) component of the momentum equation, where for each coordinate direction x_j, the artificial diffusivity d_j is positive and is chosen as the larger of zero and the local quantity μ_e (σ $Re_{\Delta x_j}$ -1)/Re. Here, the local cell Reynolds number $Re_{\Delta x_j}$ for the j-th direction is defined by

$$Re_{\Delta x_j} = Re\ |\rho u_j|\ \Delta x_j/\mu_e \tag{9}$$

This treatment lowers the formal accuracy to 0 (Δx), but the functional form is such that accuracy in representing physical shear stresses in thin shear layers with small normal velocity is not seriously degraded. This latter property follows from the anisotropic form of the dissipation and the combination of both small normal velocity

and small grid spacing in thin shear layers. A value of 0.5 was used for σ in the present calculations. Values lower than 0.5 have been used to good effect in two space dimensions [27,28], but it has not yet been possible to investigate the role of smaller σ values in three space dimensions, although it is believed that lower values of σ would also be beneficial here.

Split LBI Algorithm

Linearization and Time Differencing

The system of governing equations to be solved consists of five equations: continuity, three components of momentum and the turbulence kinetic energy equation in five dependent variables: ρ, u_1, u_2, u_3, and k. Using notation similar to that in [22], at a single grid point this system of equations can be written in the following form:

$$\partial H(\phi)/\partial t = D(\phi) + S(\phi) \tag{10}$$

where ϕ is the column-vector of dependent variables, H and S are column-vector algebraic functions of ϕ, and D is a column vector whose elements are the spatial differential operators which generate all spatial derivatives appearing in the governing equation associated with that element.

The solution procedure is based on the following two-level implicit time-difference approximations of (10):

$$(H^{n+1} - H^n)/\Delta t = \beta(D^{n+1} + S^{n+1}) + (1-\beta)\ (D^n + S^n) \tag{11}$$

where, for example, H^{n+1} denotes $H(\phi^{n+1})$ and $\Delta t = t^{n+1} - T^n$. The parameter β ($0.5 \leq \beta \leq 1$) permits a variable time-centering of the scheme, with a truncation error of order $[\Delta t^2,\ (\beta - 1/2)\ \Delta t]$.

A local time linearization (Taylor expansion about ϕ^n) of requisite formal accuracy is introduced, and this serves to define a <u>linear</u> differential operator L (cf. [22]) such that

$$D^{n+1} = D^n + L^n\ (\phi^{n+1} - \phi^n) + O\ (\Delta t^2) \tag{12}$$

Similarly,

$$H^{n+1} = H^n + (\partial H/\partial \phi)^n\ (\phi^{n+1} - \phi^n) + O\ (\Delta t^2) \tag{13}$$

$$S^{n+1} = S^n + (\partial S/\partial \phi)^n\ (\phi^{n+1} - \phi^n) + O\ (\Delta t^2) \tag{14}$$

Eqs. (12-14) are inserted into Eq. (11) to obtain the following system which is linear in ϕ^{n+1}

$$(A - \beta\Delta t\, L^n)\,(\phi^{n+1} - \phi^n) = \Delta t\,(D^n + S^n) \tag{15}$$

and which is termed a linearized block implicit (LBI) scheme. Here, A denotes a square matrix defined by

$$A \equiv (\partial H/\partial\phi)^n - \beta\Delta t\,(\partial S/\partial\phi)^n \tag{16}$$

Eq. (15) has O (Δt) accuracy unless $H \equiv \phi$, in which case the accuracy is the same as Eq. (11).

Special Treatment of Diffusive Terms

The time differencing of diffusive terms is modified to accomodate cross-derivative terms and also turbulent viscosity and artificial dissipation coefficients which depend on the solution variables. Although formal linearization of the convection and pressure gradient terms and the resulting implicit coupling of variables is critical to the stability and rapid convergence of the algorithm, this does not appear to be important for the turbulent viscosity and artificial dissipation coefficients. Since the relationship between μ_e and d_j and the mean flow variables is not conveniently linearized, these diffusive coefficients are evaluated explicitly at t^n during each time step. Notationally, this is equivalent to neglecting terms proportional to $\partial\mu_e/\partial\phi$ or $\partial d_j/\partial\phi$ in L^n, which are formally present in the Taylor expansion (12), but retaining all terms proportional to μ_t or d_j in both L^n and D^n.

It has been found through extensive experience that this has little if any effect on the performance of the algorithm. This treatment also has the added benefit that the turbulence model equations (in this instance the turbulence kinetic energy equation) can be decoupled from the system of mean flow equations by an appropriate matrix partitioning (cf. [23]) and solved separately in each step of the ADI solution procedure. This reduces the block size of the block tridiagonal systems which must be solved in each step and thus reduces the computational labor.

In addition, the viscous terms in the present formulation include a number of spatial cross-derivative terms. Although it is possible to treat cross-derivative terms implicitly within the ADI treatment which follows, it is not at all convenient to do so, and consequently, all cross-derivative terms are evaluated explicitly at t^n. For a scalar model equation representing combined convection and diffusion, it has been shown by Beam and Warming [29] that the explicit treatment of cross-derivative terms does not degrade the unconditional stability of the present algorithm. To

preserve notational simplicity, it is understood that all cross-derivative terms appearing in L^n are neglected but are retained in D^n. It is important to note that neglecting terms in L^n has no effect on steady solutions of Eq. (15), since $\phi^{n+1}-\phi^n \equiv 0$ and thus Fq. (15) reduces to the steady form of the equations: $D^n + S^n = 0$. Aside from stability considerations, the only effect of neglecting terms in L^n is to introduce an $0\ (\Delta t)$ truncation error.

Consistent Splitting of the LBI Scheme

To obtain an efficient algorithm, the linearized system (15) is split using ADI techniques. To obtain the split scheme, the multidimensional operator L is rewritten as the sum of three "one-dimensional" sub-operators L_i (i = 1, 2, 3) each of which contains all terms having derivatives with respect to the i-th spatial coordinate. The split form of Eq. (15) can be derived either as in [22, 23] by following the procedure described by Douglas and Gunn]24] in their generalization and unification of scalar ADI schemes, or using approximate factorization as in [25]. For the present system of equations, the split algorithm is given by

$$(A - \beta\Delta t L_1^n)\ (\phi^* - \phi^n) = \Delta t\ (D^n + S^n) \tag{17a}$$

$$(A - \beta\Delta t L_2^n)\ (\phi^{**} - \phi^n) = A\ (\phi^* - \phi^n) \tag{17b}$$

$$(A - \beta\Delta t L_3^n)\ (\phi^{n+1} - \phi^n) = A\ (\phi^{**} - \phi^n) \tag{17c}$$

where ϕ^* and ϕ^{**} are consistent intermediate solutions [22,]2]. If spatial derivatives appearing in L_i and D are replaced by three-point difference formulas, as indicated previously, then each step in Eqs. (17a-c) can be solved by a block-tridiagonal elimination.

Combining Eqs. (17a-c) gives

$$(A - \beta\Delta t L_1^n)\ A^{-1}\ (A - \beta\Delta t L_2^n)\ A^{-1}\ (A - \beta\Delta t L_3^n)\ (\phi^{n+1} - \phi^n) = \Delta t\ (D^n + S^n) \tag{18}$$

which approximates the unsplit scheme (15) to $0\ (\Delta t^2)$. Since the intermediate steps are also consistent approximations for Eq. (15', physical boundary conditions can be used for ϕ^* and ϕ^{**} [22, 23]. Finally, since the L_i are homogeneous operators, it follows from Eqs. (17a-c) that steady solutions have the property that $\phi^{n+1} = \phi^* = \phi^{**} = \phi^n$ and satisfy

$$D^n + S^n = 0 \tag{19}$$

The steady solution thus depends only on the spatial difference approximation used for (19) and does not depend on the solution algorithm itself.

COMPUTED RESULTS

Solutions for three-dimensional laminar and turbulent flow in 90-degree bends having strong curvature and both circular and square cross sections are presented here. To assess the degree of accuracy obtainable in this type of three-dimensional flow calculation, it is obviously valuable to have experimental measurements for comparison. Fortunately, laser-Doppler anemometry measurements have recently become available [7, 8, 12, 13] for several laminar and turbulent square duct and pipe bends. Computed results for six different flow cases are included here, and the relevant flow parameters describing these cases are given in Table I. Each of the three bend geometries considered is shown to scale in Fig. 3. The cases include both laminar and turbulent flow in a pipe bend of curvature 2.8 (cases 1 and 2) and in a square duct of curvature 2.3 (cases 4 and 5). Measurements are given by Taylor, Whitelaw and Yianneskis both for the pipe bend [13] and for the curved duct [12].

TABLE I - PARAMETERS FOR 90-DEGREE BEND CALCULATIONS

Case	Type	Re_d	Curvature R/d	Upstream Extension d	Downstream Extension d	Inlet Boundary Layer Thickness δ/d	Grid x_1, x_2, x_3	Minimum Mesh Spacing $\Delta x/d$
1	Laminar Pipe Bend	500	2.8	2.0	2.0	0.363	28x18x19	0.0037
2	Turbulent Pipe Bend	43,000	2.8	2.0	2.0	0.15	28x18x19	0.00183
3	Turbulent Pipe Elbow	43,000	1.0	2.0	4.83	0.15	28x18x19	0.00183
4	Laminar Square Duct	790	2.3	4.0	4.0	0.365	28x16x21	0.00426
5	Turbulent Square Duct	40,000	2.3	1.5	1.65	0.2	28x13x16	0.00264
6	Turbulent Square Duct	40,000	2.3	8.2	2.0	0.5	28x13x25	0.00278

The other cases include a pipe elbow configuration (Case 3), which has a curvature of 1.0, but is otherwise identical to Case 2, and a curved duct (Case 6) which is identical to Case 5 except that it has a nominally fully-developed inflow velocity profile. The latter flow case was measured by Humphrey, Taylor and Whitelaw [8] and was included as one of the evaluation cases for the 1980-81 Stanford conference on Complex Turbulent Flows.

A vast amount of information is obtained from the computation of six three-dimensional flow cases, and only selected, representative results can be included here. The present approach to this problem is as follows: First, the computed axial velocity is compared with experimental measurements in each of the five cases for which data is available. Next, each of the three pipe bend cases (1 - 3) is presented in a sequence of plots designed to show the developing flow structure. The structure of square-duct flows was considered in more detail in [10, 11]. Finally, a comparison is made of the two turbulent curved duct flows which differ only in the inflow boundary layer thickness.

Convergence Rate

Before proceeding to the discussion of computed flow behavior, an indication is given of the degree and rate of convergence obtained in these calculations. Turbulent flows, particularly in three dimensions, are especially difficult to compute because of the very high degree of mesh redistribution required to resolve viscous sublayer regions. Since peak secondary flow velocities often occur within or near the viscous sublayer, resolution of the viscous sublayer is believed necessary to obtain an adequate representation of the overall flow, but poses a computational problem for which rapid convergence is difficult to achieve. The complicated flow structure in curved ducts and pipes, which includes strong secondary flows and their resulting distortion of the primary flow, also contributes to the difficulty of these flows.

The present computational method employs variable time steps to accelerate convergence, as discussed in [30]. Several procedures for time step selection are presently under evaluation, but typically small time steps are used initially during the elimination of impulsive transients, followed by larger time steps and the cyclic use of a sequence of time steps. In addition, a smaller time step was used near the leading edge than elsewhere in the flow field. Small time steps are effective in reducing high (spatial) frequency error components, while large time steps are effective in reducing low frequency errors.

An indication of both the degree and rate of convergence obtained for the three-pipe flow calculations (which are representative cases) is shown in Fig. 4. For comparison, a curve representative of the convergence behavior typically obtained for two-dimensional turbulent flow cases is also shown. Although the present convergence rate is noticeably slower than that observed using this same algorithm in other calculations, it is adequate for present purposes. The present calculations were terminated as shown in Fig. 4. for reasons of economy, since it appeared that the observed changes in the solution at this point were of minor significance and would not alter any of the conclusions drawn from these results.

Comparison With Experiment

Computed contours of axial velocity are compared with experimental measurements in Figs. 5 - 9. To aid in the comparison, contour values shown for the computed solutions are the same as has been shown for the measuremtns. The computed velocities were normalized by the mean (bulk) velocity as determined by a second-order numerical integration of the computed solution. This calculation indicated that global mass conservation was satisfied by all computed solutions to within one per cent at each axial location. In comparing these results with the measurements, the normalized mass flux (as evidenced by peak and centerline velocity) did not appear to match in some cases. To aid in the comparison, the computed contours shown in Figs. 5 - 9 were renormalized to provide a nominal matching of centerline velocity at the first measured station. Downstream stations were adjusted by this same factor. This renormalization led to adjustment of the computed velocities by the following amounts: Case 2 - 3.6%, Case 4 - 7.4%, Case 6 - 4%. No adjustment was required for Case 1, and the computed mass flux was not checked for Case 5.

All of the flow cases considered here develop strong secondary flows as a result of turning and these secondary flows result in considerable distortion of the primary flow, particularly near the inside of the bend. This distortion of the primary flow is the principal method of judging the agreement between measured and computed results in Figs. 5 - 9. Both a comparison of the duct flows with two-dimensional channel flow having the same curvature and also limited mesh refinement studies were given in a previous study [10, 11].

In Fig. 5, the computed results for laminar pipe flow are in very good general agreement with the measurements. The turbulent pipe flow predictions in Fig. 6 also agree reasonably well with measurements, although the predicted flow distortion is

somewhat less localized than that measured. Since the laminar calculations employ no physical assumptions beyond those of the Navier-Stokes equations, the level of agreement is indicative of the numerical truncation error and experimental error. The difference between the level of agreement for laminar and turbulent predictions is at least partly an indication of error in the turbulence model. The predictions for the three duct flow cases in Figs. 7 - 9 are in good qualitative and reasonable quantitative agreement with the measurements, although the agreement is not as good as was obtained in the pipe flow cases. This may be partly due to the increased difficulty of grid resolution (cf. Fig. 2) in the center of the duct, since two grid-stretching transformations are needed for the square cross section, as opposed to one for the circular pipe. It is also worth noting that the computed velocity contours in Fig. 9a in the straight section 2.5 duct widths upstream of the bend do not display the "corner distortion" found in the measurements. This distortion is the result of weak "stress driven" secondary flows, and its absense in the computed results is attributed to the assumption of an isotropic turbulent viscosity in the turbulence model.

Flow Structure for Pipe Bend Cases

A sequence of plots is given in Figs. 10 - 15 for each of the three pipe flow cases. These figures are designed to show the flow structure as it develops at successive axial locations for each computed solution, the axial distribution of pressure coefficient referred to reference conditions and bulk velocity at the inner and outer wall locations in the plane of the centerline is first given. The pressure coefficient provides an indication of the extent of influence of the flow in the bend on the flow in the upstream and downstream straight extensions. The distribution of grid points is included in these plots. Also shown is the difference in pressure coefficient, Δc_p, which would occur for a potential flow with velocity inversely proportional to radius, in a bend of the same curvature.

Following the pressure coefficient, a sequence showing the primary and secondary velocity distributions at successive axial locations is given. The same contour values are shown throughout Figs. 10 - 15; the vector magnitudes are renormalized for each plot and thus indicate only flow direction and relative magnitude within each plot. The strength of the secondary flows is shown by giving the magnitude of the peak velocity, VMAX, within the vector plot.

Comparing the laminar and turbulent cases in Figs. 10 - 13, the laminar flow is seen to have a mush larger pressure drop (viscous loss) and higher peak axial velocity than the turbulent case. The secondary flows are of similar strength, reaching about 40 per cent of the mean axial velocity. The turbulent pipe elbow case (Figs. 14, 15) has an inflow identical to that of Case 2, but there are considerable differences in flow development, as a result of the strong curvature. The radial pressure gradient across the bend is very large (Fig. 14), and the secondary velocities are over 60 per cent of the mean axial velocity. In addition, the peak axial velocity is larger (≈ 1.6) than the 2.3 curvature case, and occurs near the inside of the bend rather than the outside. Somewhat surprisingly, the only flow separation present was of very limited extent and is not visable in the plots. This occurred near the 90-degree location, on the inner side of the pipe bend.

Influence of Boundary Layer Thickness on Duct Flow

The axial and secondary velocity distributions at 60 and 90 degrees are compared in Figs. 16 - 17 for the two turbulent duct flows (Cases 5, 6) with different inlet boundary layer thickness, δ_{in}. The computed flow structure is not very sensitive to this parameter, and the most notable difference is that the distortion of the axial velocity produces a thinner shear layer on the outer wall for case 6 with $\delta_{in} = 0.5$. Finally, the pressure coefficient for these two cases is shown in Fig. 18. The pressure field remains largely two dimensional, although there is some three-dimensional distortion associated with the corner vortex flow on the inside of the bend.

CONCLUDING REMARKS

Three-dimensional laminar and turbulent flow within 90-degree bends of strong curvature and both circular and square cross section has been studied by numerical solution of the compressible Reynolds-averaged Navier-Stokes equations. Straight extensions upstream and downstream of the bend are included in the computed flow region. It is believed that the physical processes involved require the viscous sublayer to be resolved, and the computational approach provides for this resolution. Six different flow cases were considered, and the results were evaluated by comparison with experiment measurements. In general, very good qualitative and reasonable quantitative agreement between solution and experiment was observed. The developing flow structure and its dependence on geometric and flow parameters was also studied.

Collectively, this sequence of experimental comparisons helps to establish the accuracy with which these flows can be predicted by the present method using moderately coarse grids ($\approx$ 10,000 grid points). With some allowance made for the complexity of the flow and the difficulty of both computing and measuring flows of this type, the agreement between computed and measured results is regarded as generally very good. The sources of disagreement are believed attributable to numerical truncation error and to a lesser extent the turbulence model.

REFERENCES

1. Hawthorne, W.R.: The Applicability of Secondary Flow Analyses to the Solution of Internal Flow Problems, Fluid Mechanics of Internal Flow, ed. G. Sovran, (Elsevier), 1967, p. 263.

2. Hawthorne, W.R.: Research Frontiers in Fluid Dynamics, eds. R.J. Seeger and G. Temple, (Interscience), 1965, p. 1.

3. Horlock, J.H. and Lakshminarayana, B.: Secondary Flows; Theory, Experiment and Application in Turbomachinery Aerodynamics, Annual Rev. Fluid Mech., Vol. 5, 1973, p. 247.

4. Pratap, V.S. and Spalding, D.B.: Fluid Flow and Heat Transfer in Three-Dimensional Duct Flows, Int. J. Heat & Mass Transfer, Vol. 19, 1976, p. 1183.

5. Ghia, K.N. and Sokhey, J.S.: Laminar Incompressible Viscous Flow in Curved Ducts of Rectangular Cross-Sections, J. Fluid Engr., Vol. 99, 1977, p. 640.

6. Kreskovsky, J.P., Briley, W.R. and McDonald, H.: Prediction of Laminar and Turbulent Primary and Secondary Flows in Strongly Curved Ducts, NASA CR-3388, February 1981.

7. Humphrey, J.A.C., Taylor, A.M.K. and Whitelaw, J.H.: Laminar Flow in a Square Duct of Strong Curvature, J. Fluid Mech., Vol. 83, 1977, p. 509.

8. Humphrey, J.A.C., Whitelaw, J.H. and Yee, G.: Turbulent Flow in a Square Duct with Strong Curvature, J. Fluid Mech., 103, 443, 1981.

9. Yee, G. and Humphrey, J.A.C.: Developing Laminar Flow and Heat Transfer in Strongly Curved Ducts of Rectangular Cross-Section. ASME Paper 79-WA/HT-15, 1979.

10. Buggeln, R.C., Briley, W.R. and McDonald, H.: Computation of Laminar and Turbulent Flow in Curved Ducts, Channels and Pipes Using the Navier-Stokes Equations, SRA Report R80-920006-F, December 1980.

11. Buggeln, R.C., Briley, W.R. and McDonald, H.: Solution of the Navier-Stokes Equations for Three-Dimensional Turbulent Flow with Viscous Sublayer Resolution. AIAA Paper No. 81-1023, 1981.

12. Taylor, A.M.K.P., Whitelaw, J.H. and Yianneskis, M.: Measurements of Laminar and Turbulent Flow in a Curved Duct with Thin Inlet Boundary Layers, Imperial College Report FS/80/29, 1980.

13. Taylor, A.M.K.P., Whitelaw, J.H. and Yianneskis, M.: Curved Ducts with Secondary Motion; Velocity Measurements of Developing Laminar and Turbulent Flow (to be published in J. Fluid Engineering).

14. Hughes and Gaylord: Basic Equations of Engineering Science. Schaum Publishing Co.

15. Roberts, G.O.: Computational Meshes for Boundary Layer Problems. Proc. 2nd Int. Conf. Num. Meth. Fluid Dynamics, (Springer-Verlag), 1971, p. 171.

16. Launder, B.E. and Spalding, D.B.: Mathematical Models of Turbulence. Academic Press, 1972.

17. Shamroth, S.J. and Gibeling, H.J.: The Prediction of the Turbulent Flow Field About an Isolated Airfoil, AIAA Paper 79-1543, 1979. Also, NASA CR-3183, 1979.

18. Launder, B.E. and Spalding, D.B.: The Numerical Computation of Turbulent Flows. Computer Methods in Applied Mechanics and Engineering, Vol. 3, 1974, p. 269.

19. McDonald, H. and Fish, R.W.: Practical Calculations of Transitional Boundary Layers. International Journal of Heat and Mass Transfer, Vol. 16, No. 9, 1973, pp. 1729-1744.

20. McDonald, H. and Briley, W.R.: Some Observations on Numerical Solutions of the Three-Dimensional Navier-Stokes Equations. Symposium on Numerical and Physical Aspects of Aerodynamic Flows. Cal. State Univ. (Long Beach), 1981.

21. Musker, A.J.: Explicit Expression for the Smooth Wall Velocity Distribution in a Turbulent Boundary Layer. AIAA Journal, Vol. 17, 1979, p. 655.

22. Briley, W.R. and McDonald, H.: Solution of the Multidimensional Compressible Navier-Stokes Equations by a Generalized Implicit Method. J. of Comp. Physics, Vol. 234, Aug. 1977, p. 372.

23. Briley, W.R. and McDonald, H.: On the Structure and Use of Linearized Block ADI and Related Schemes. J. Comp. Physics, Vol. 34, 1980, p. 54.

24. Douglas, J. and Gunn, J.E.: A General Formulation of Alternating Direction Methods. Numerische Math., Vol. 6, 1964, p. 428.

25. Beam, R.M. and Warming, R.F.: An Implicit Factored Scheme for the Compressible Navier-Stokes Equations. AIAA Journal, Vol. 16, April 1978, p. 393.

26. Beam, R.M. and Warming, R.F.: An Implicit Finite-Difference Algorithm for Hyperbolic Systems in Conservation Law Form. Journal of Computational Physics, Vol. 22, Sept. 1976, p. 87.

27. Shamroth, S.J., McDonald, H. and Briley, W.R.: A Navier-Stokes Solution for Transonic Flow Through a Cascade. SRA Report R79-920007-F, 1979.

28. McDonald, H., Shamroth, S.J. and Briley, W.R.: Transonic Flows with Viscous Effects. Transonic Shock and Multidimensional Flows: Advances in Scientific Computing. R.E. Meyer, Ed., Academic Press, New York, 1982.

29. Beam, R.M. and Warming, R.F.: Alternating Direction Implicit Methods for Parabolic Equations with a Mixed Derivative. SIAM J. Sci. Stat. Comp., Vol. 1, 1980, p. 131.

30. McDonald, H. and Briley, W.R.: Computational Fluid Dynamic Aspects of Internal Flows. AIAA Paper No. 79-1445, 1979.

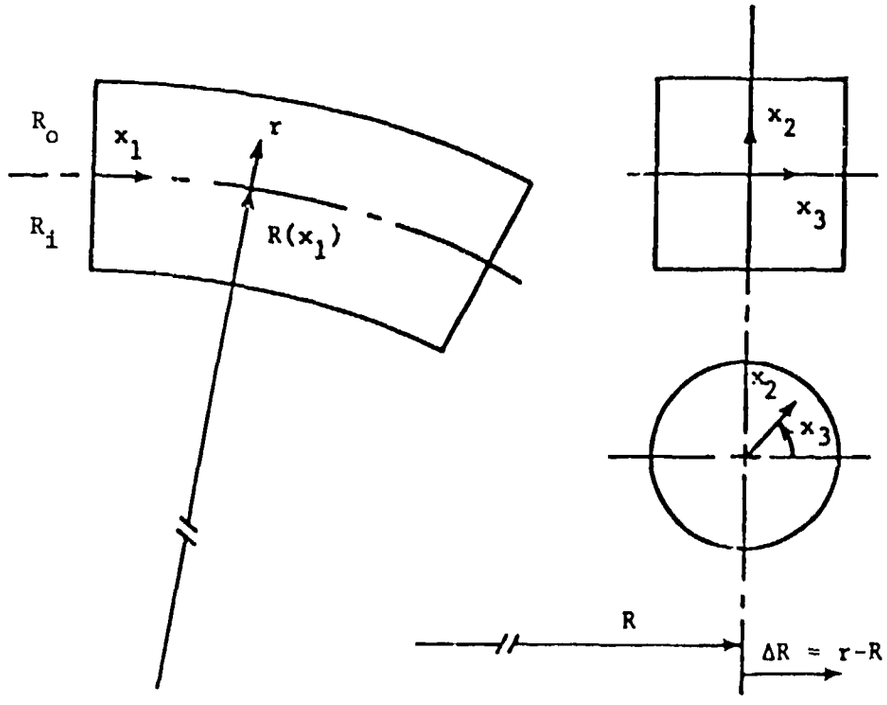

(a) Plane of Centerline Curvature

(b) Plane Normal to Centerline

Fig. 1 - Schematic of Coordinate System.

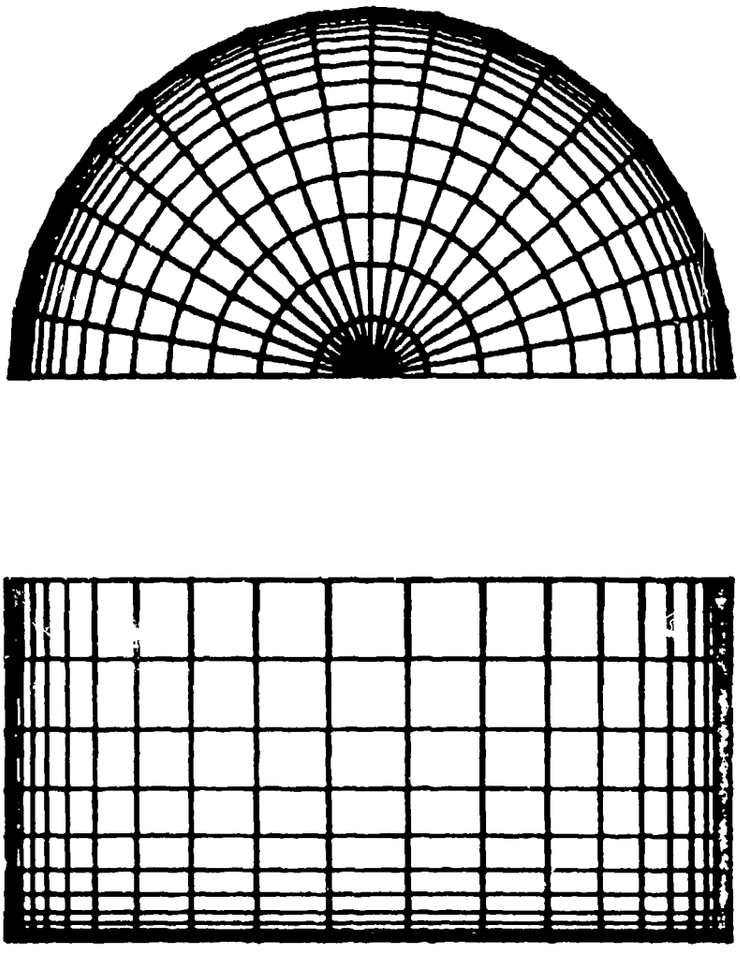

Fig. 2 - Representative Grids in Cross Sectional Plane.

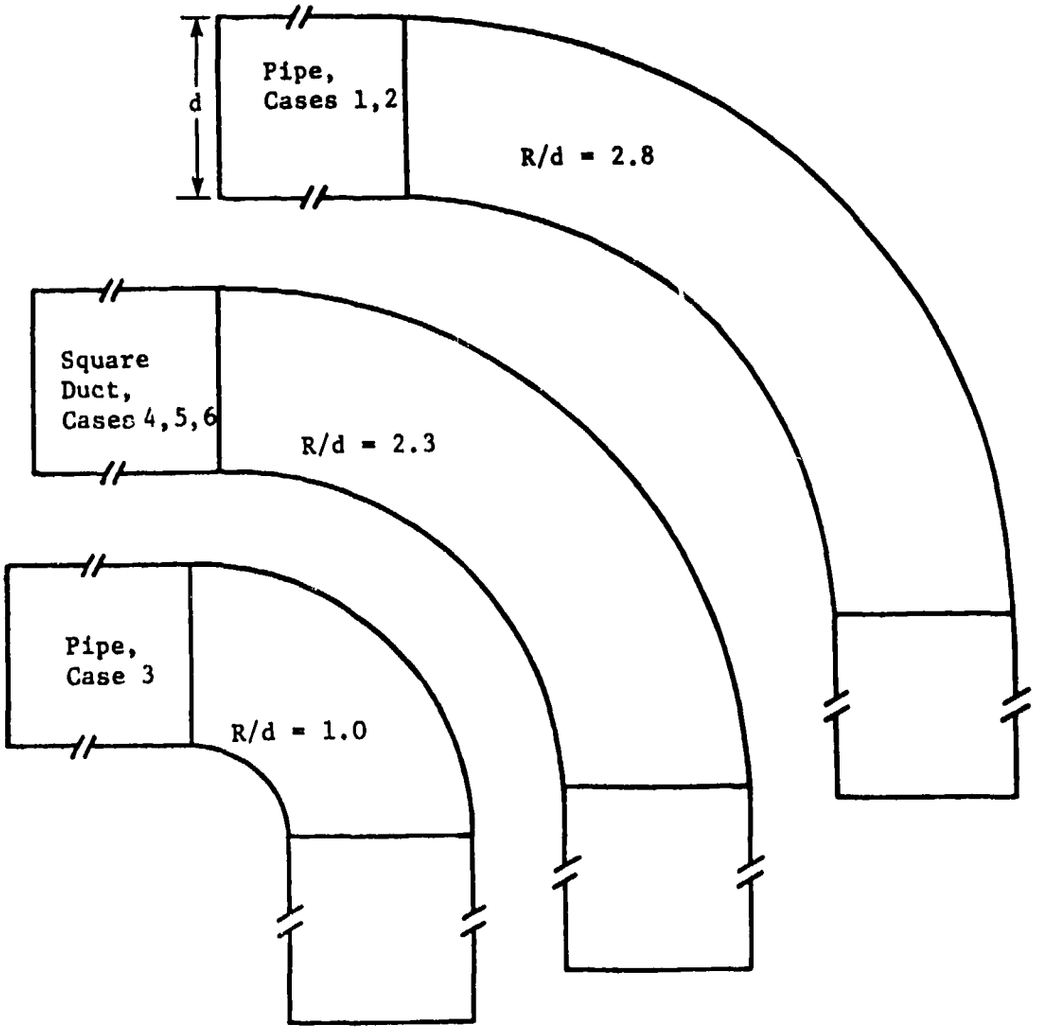

Fig. 3 - Bend Geometries (to scale).

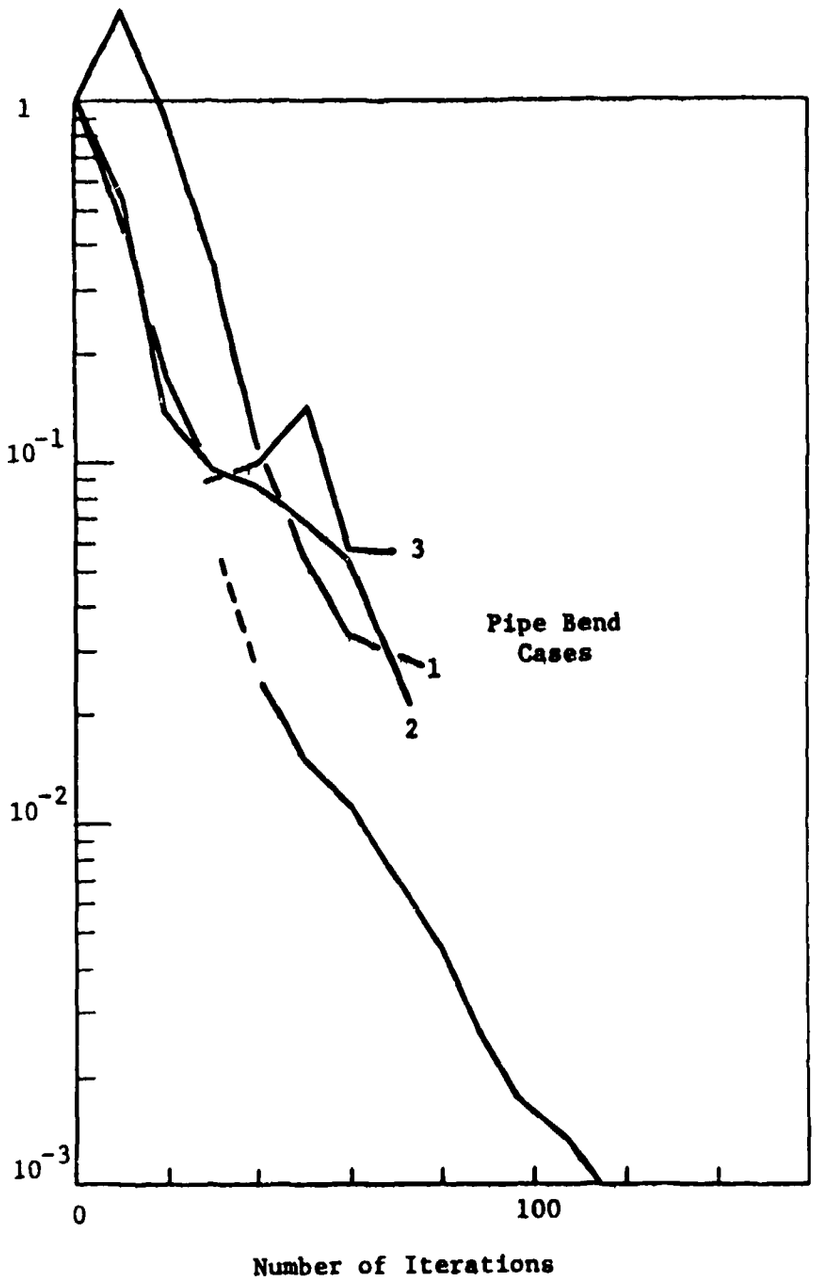

Fig. 4 - Convergence Rate for Selected Cases.

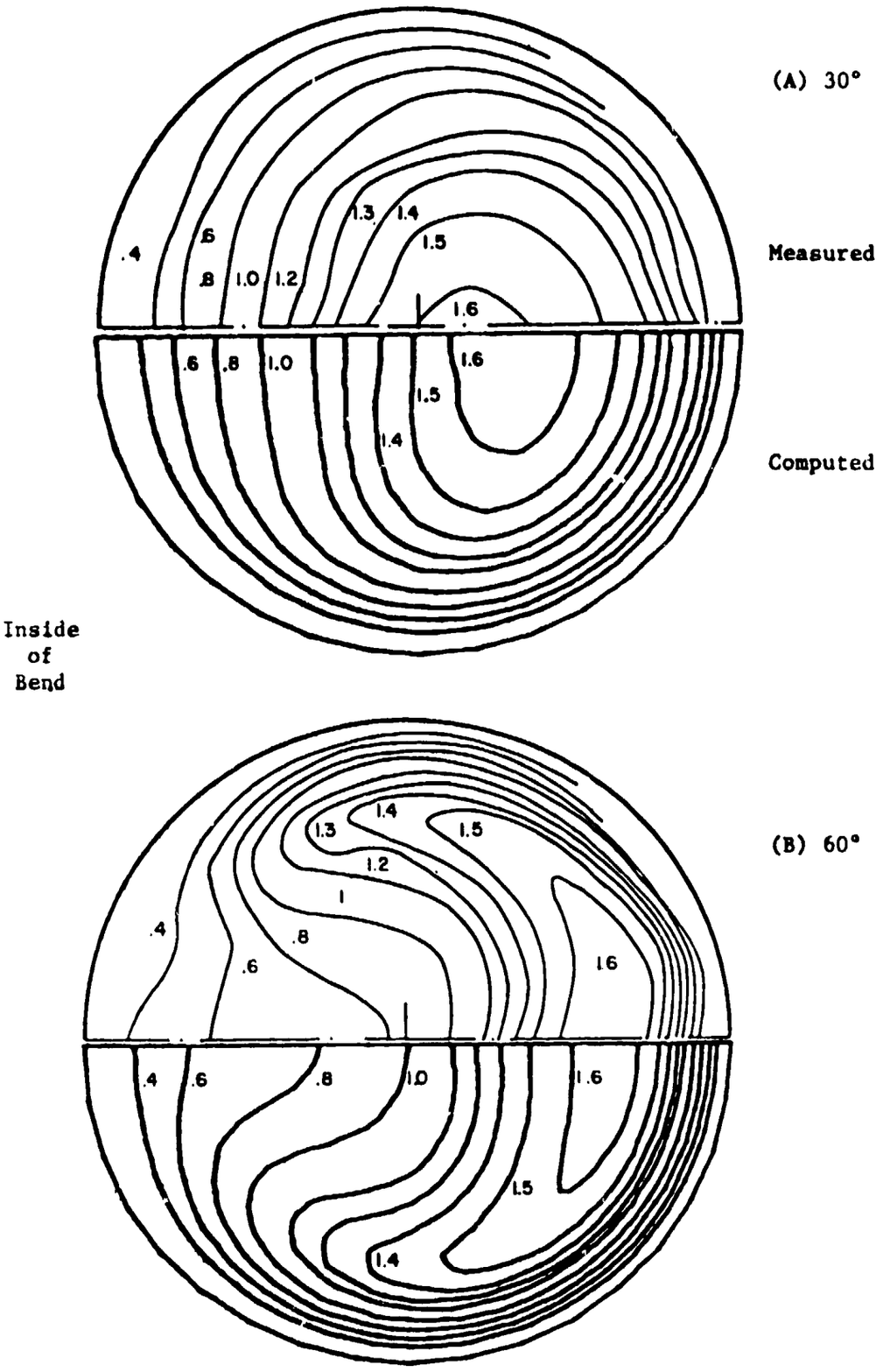

Fig. 5 - Laminar Pipe Bend (Case 1 - Re = 500, R/d = 2.8). Axial Velocity Compared with Measurements of [13].

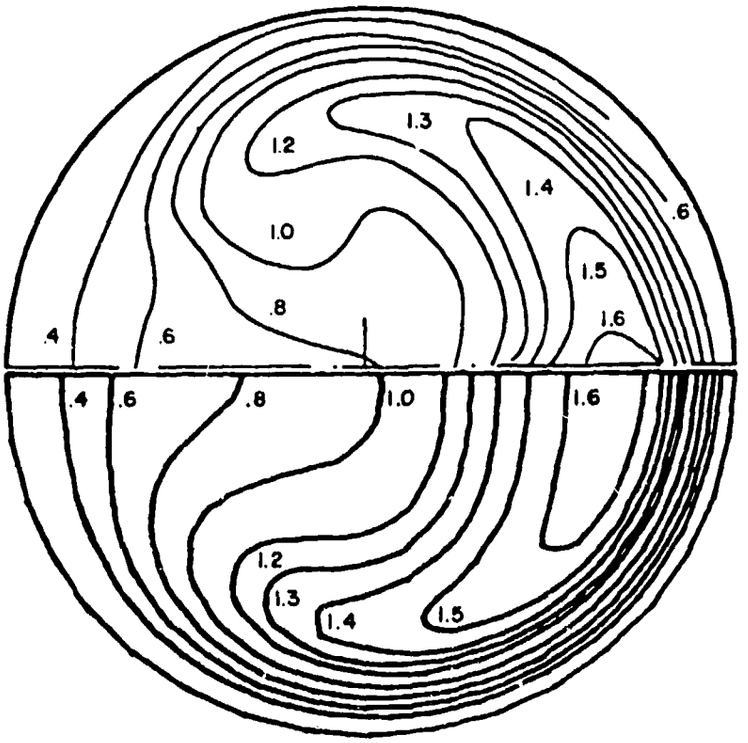

(C) 75°

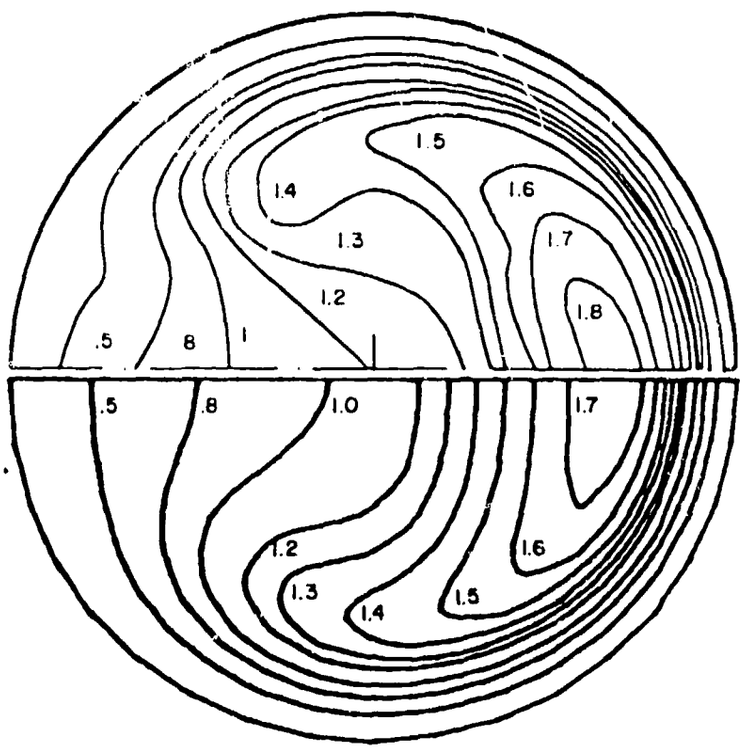

(D) + 1.0

Fig. 5 - (Continued)

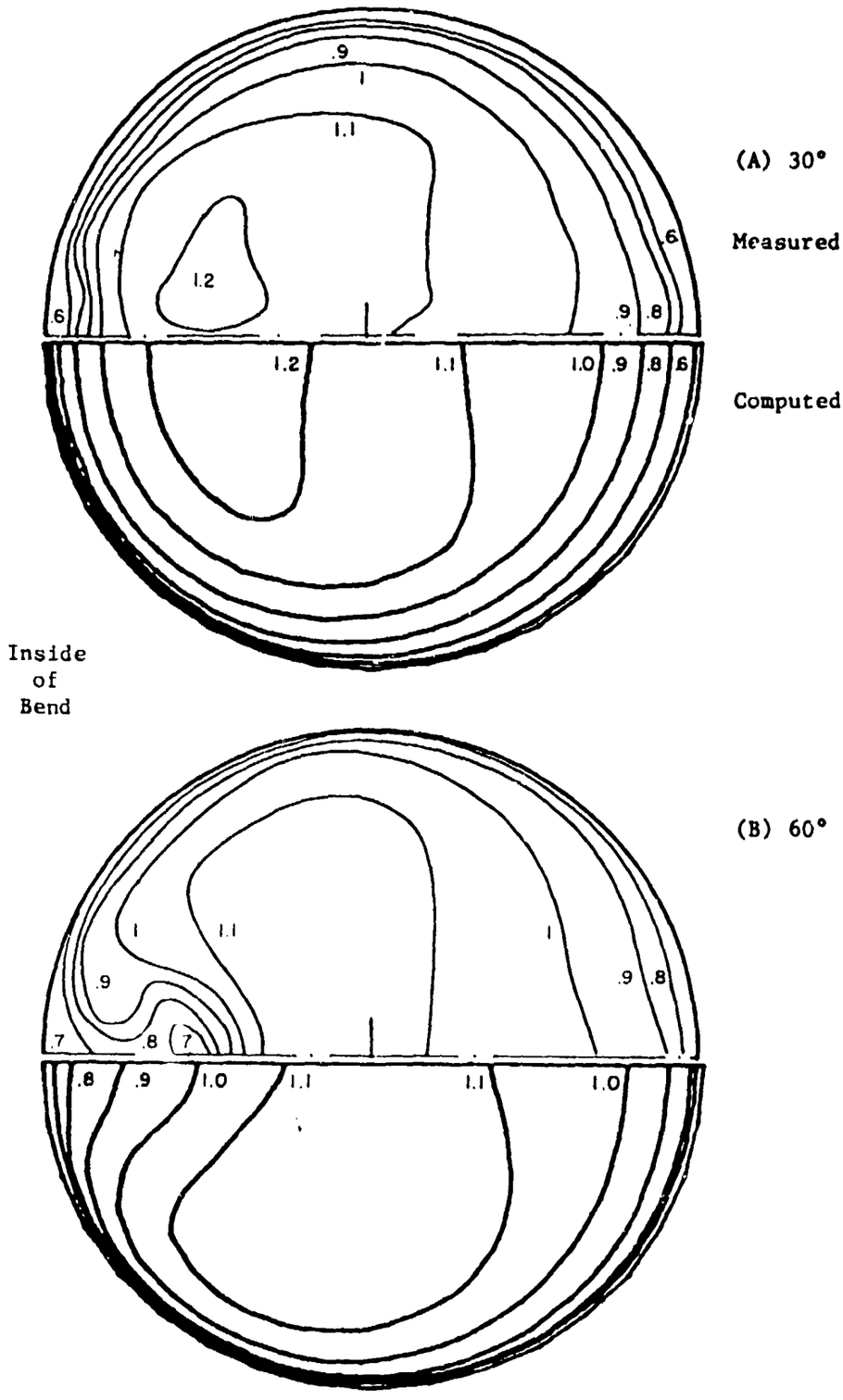

Fig. 6 - Turbulent Pipe Bend (case 2 - Re = 43,000, R/d = 2.8). Axial Velocity Compared with Measurements of [13].

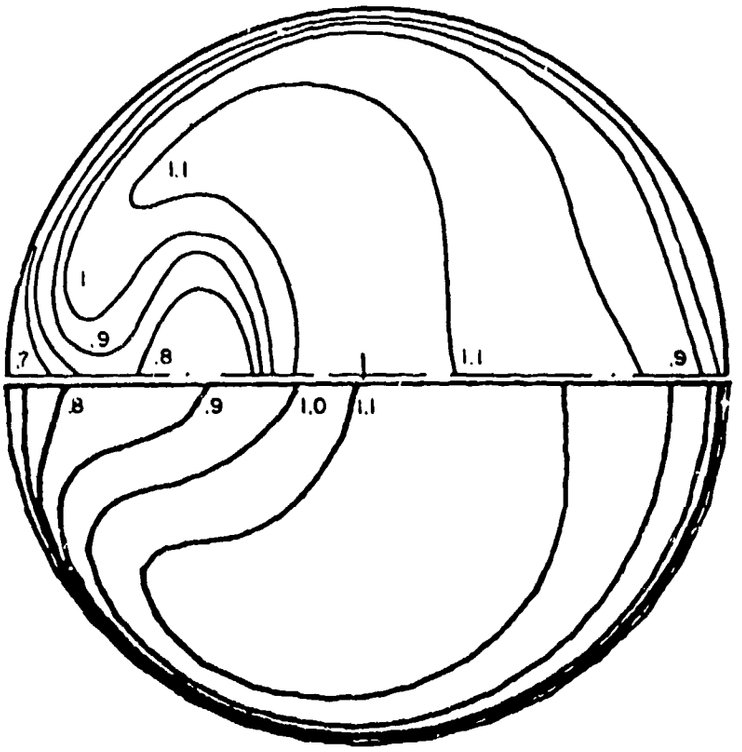

(C) 75°

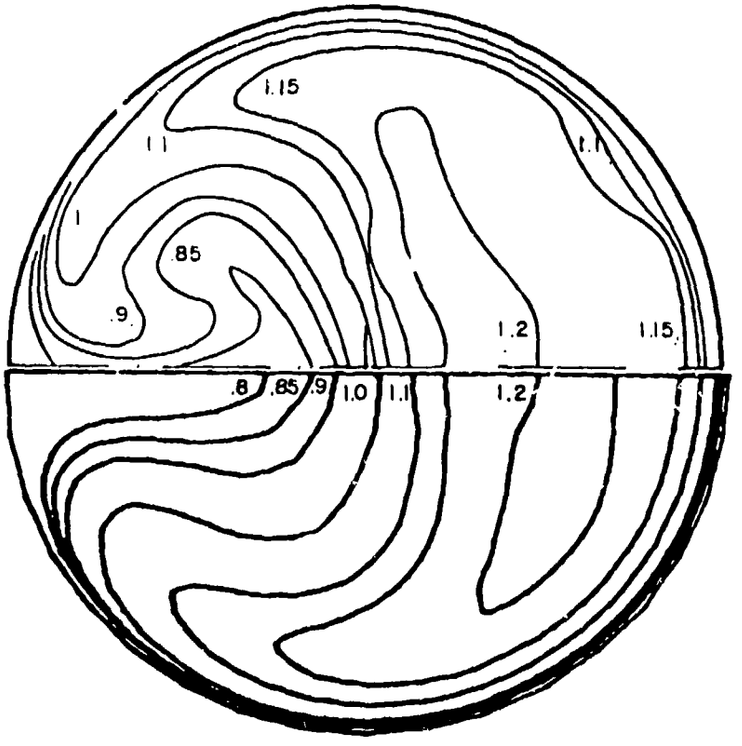

(D) + 1.0

Fig. 6 (Continued)

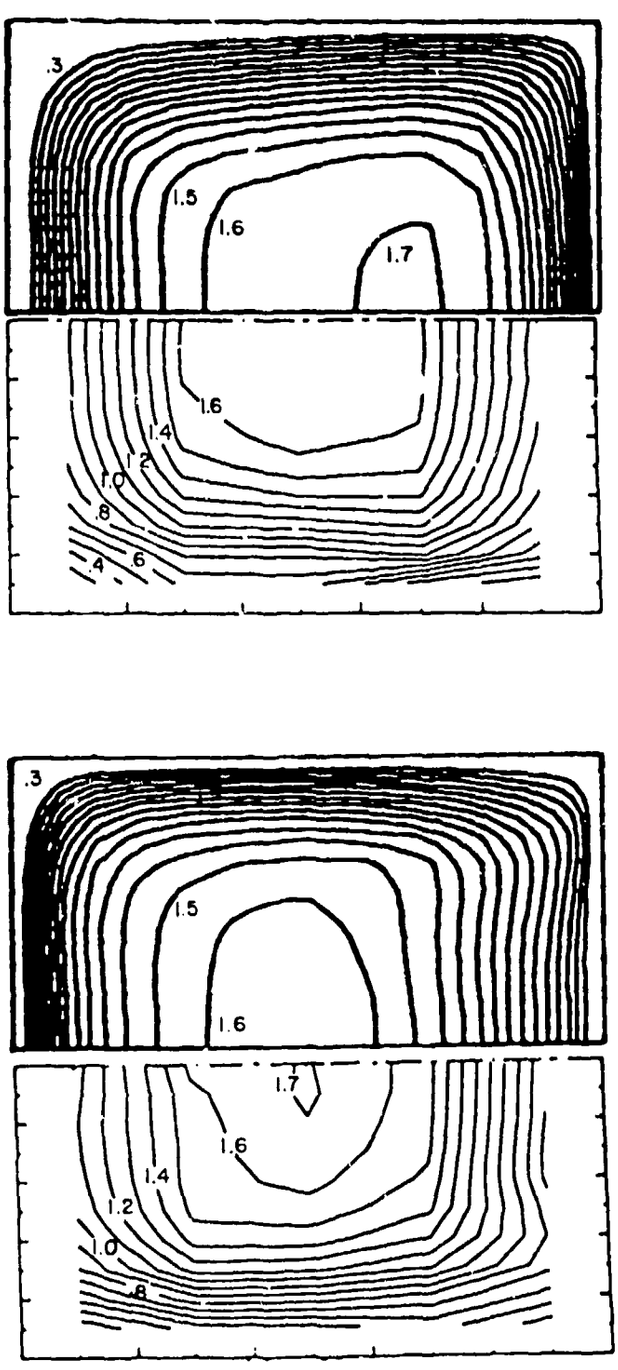

Fig. 7 - Laminar Duct Bend (Case 4 - Re = 790, R/d = 2.3). Axial Velocity Compared with measurements of [12].

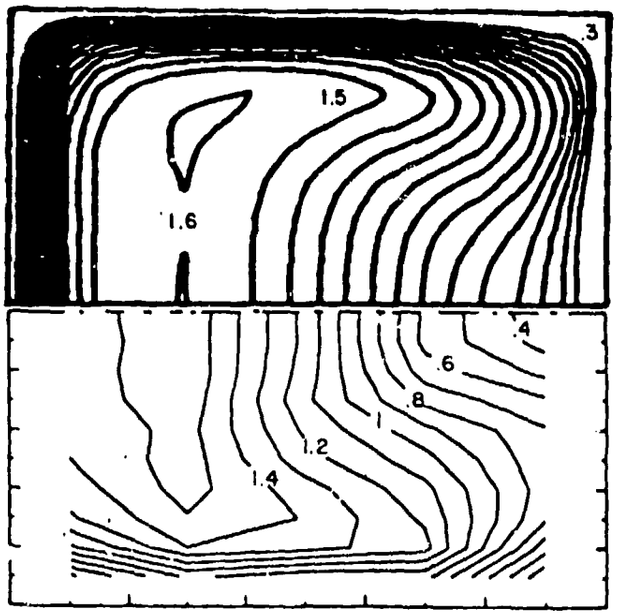

(C) 60°

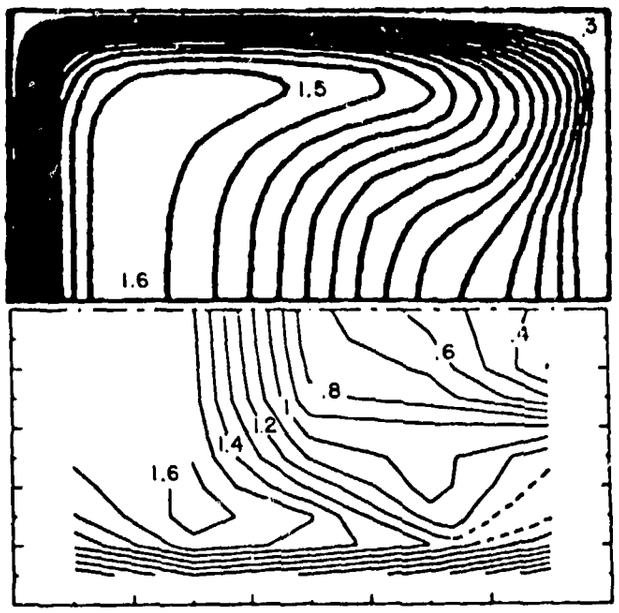

(D) 77.5°

Fig. 7 (Continued)

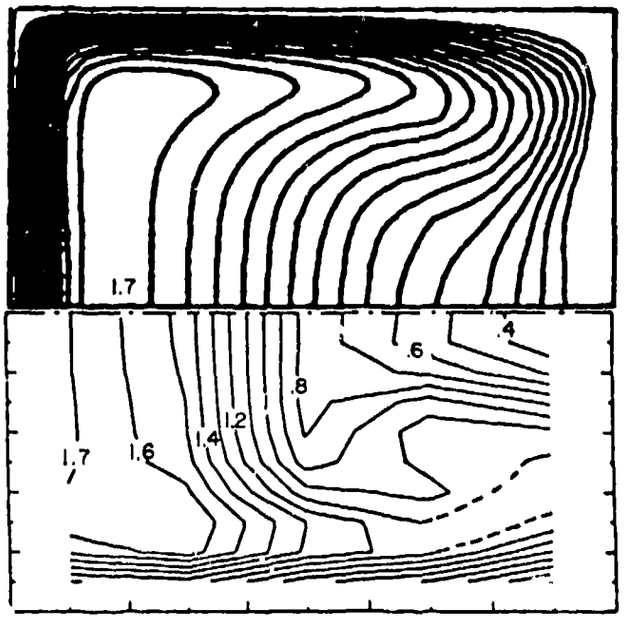

(E) +0.25

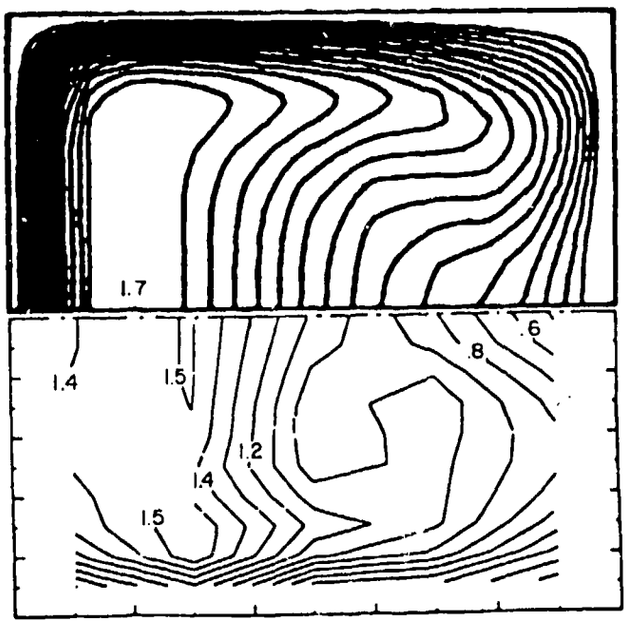

(F) +2.5

Fig. 7 (Continued)

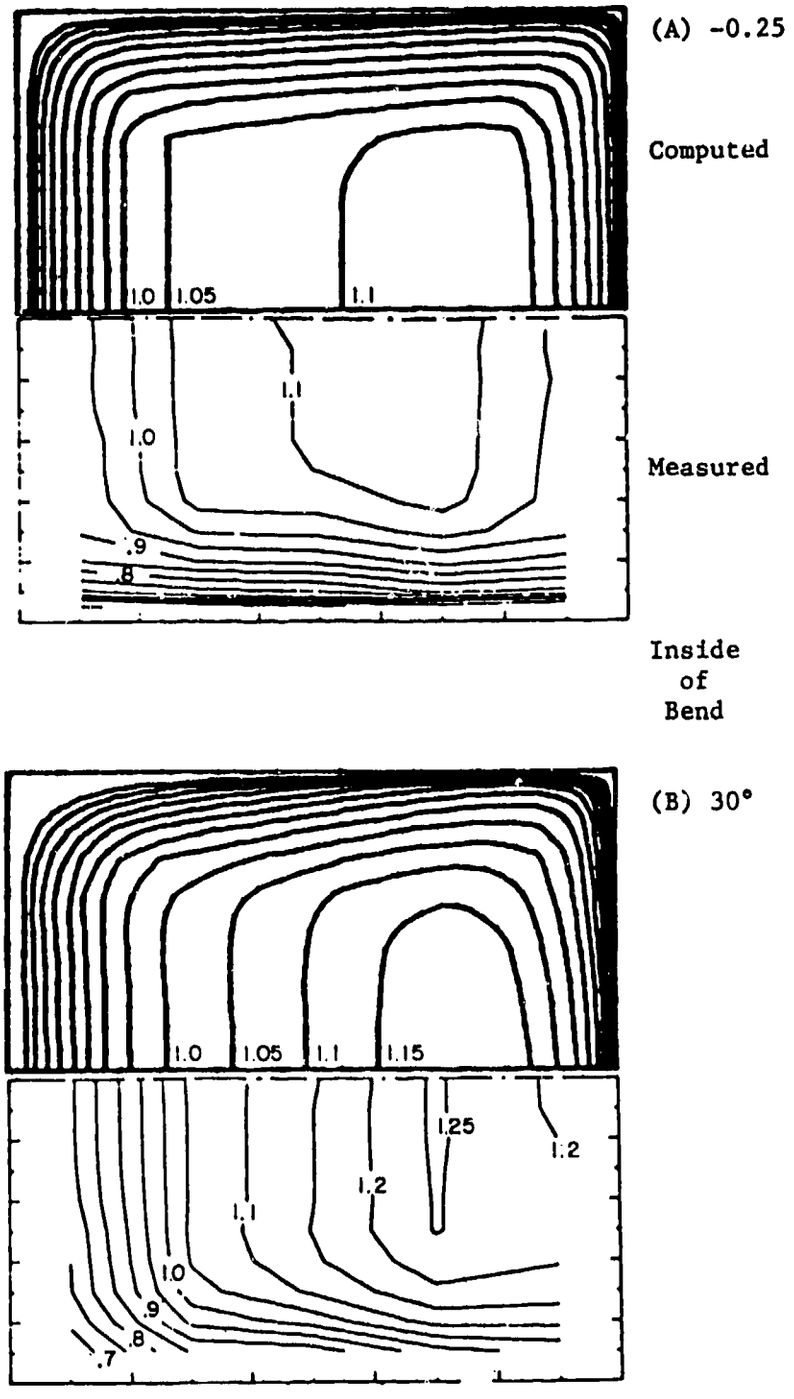

Fig. 8 - Turbulent Duct Bend (Case 5 - Re = 40,000, R/d = 2.3). Axial Velocity Compared with Measurements of [12].

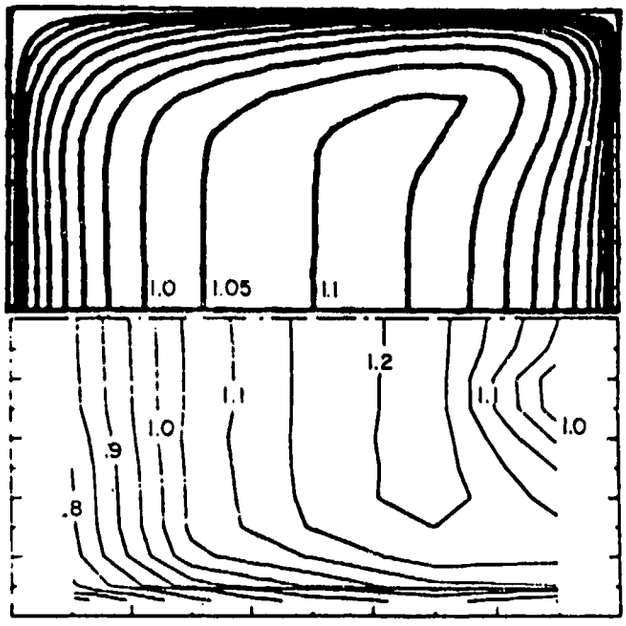

(C) 60°

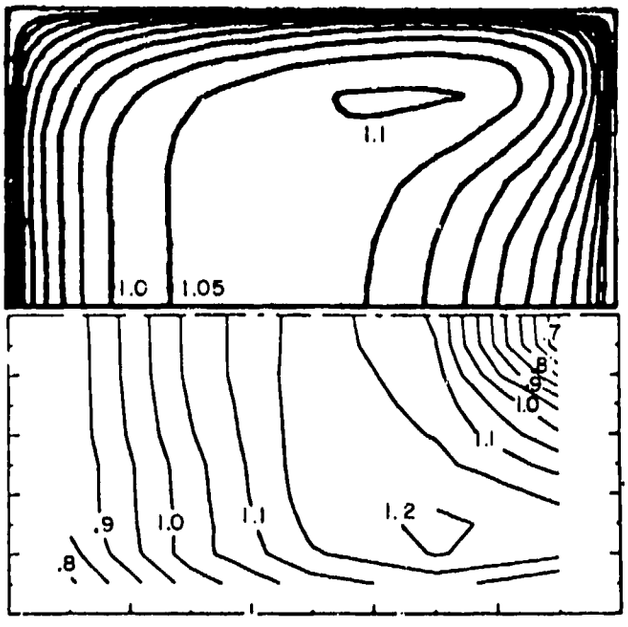

(D) 77.5°

Fig. 8 (Continued)

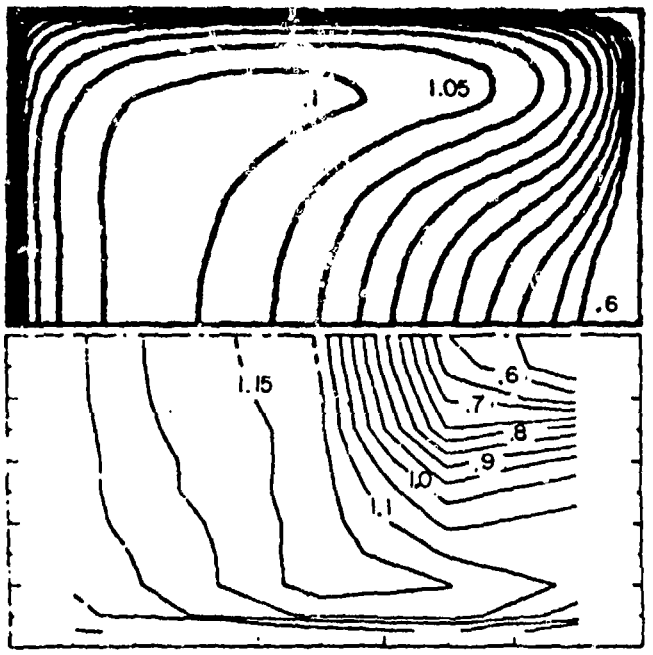

(E) +0.25

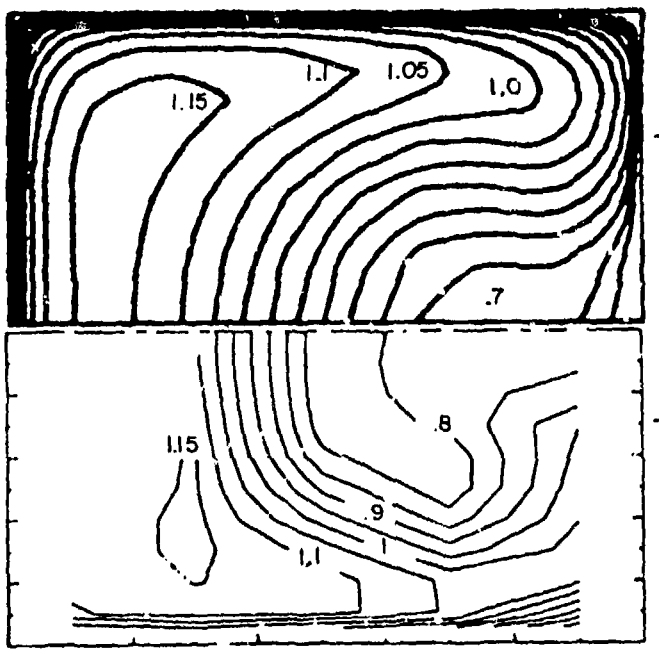

(F)

+1.65

+2.5

Fig. 8 (Continued)

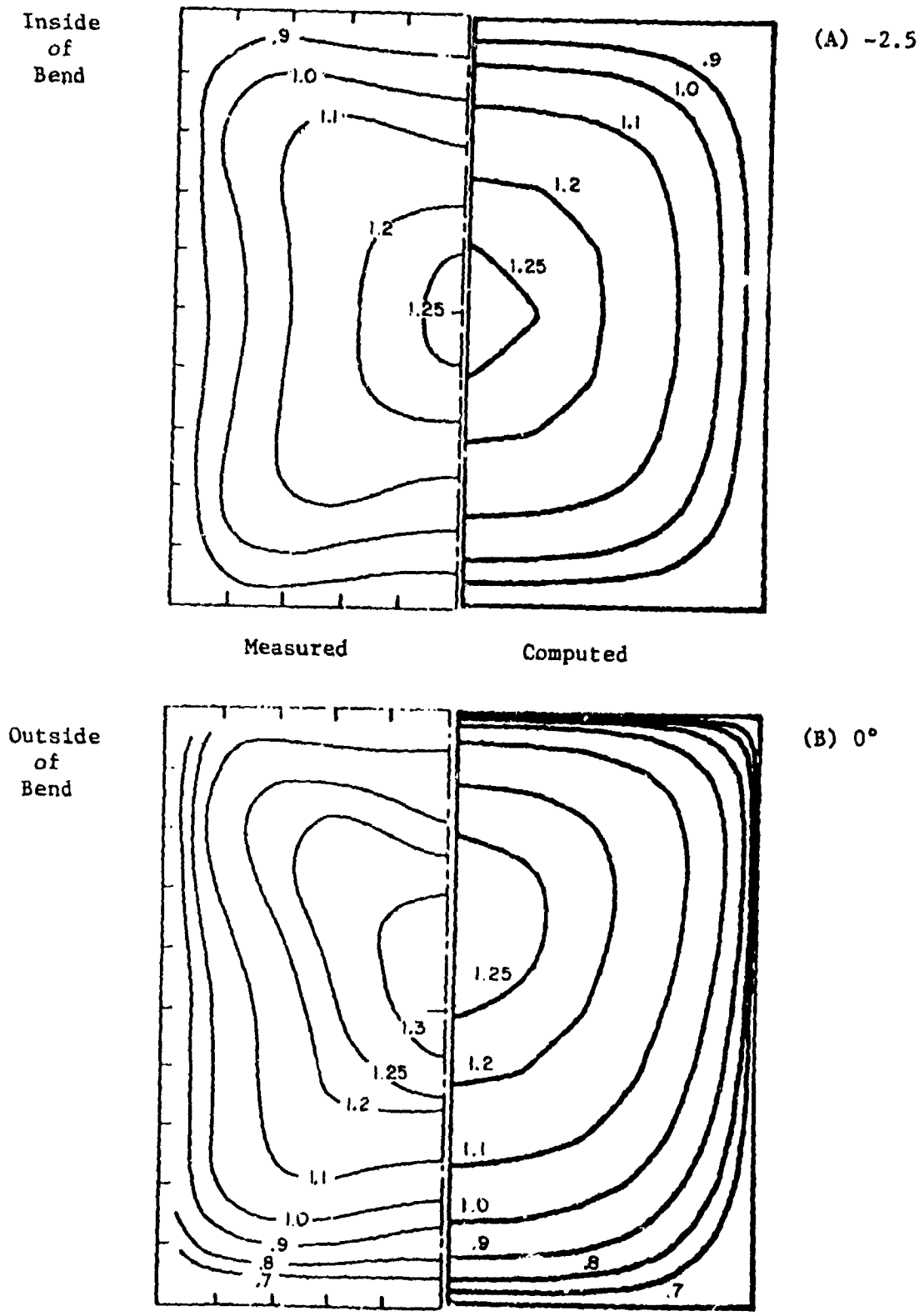

Fig. 9 - Turbulent Duct Bend (Case 6 - Re = 40,000, R/d = 2.3). Axial Velocity Compared with Measurements of [8].

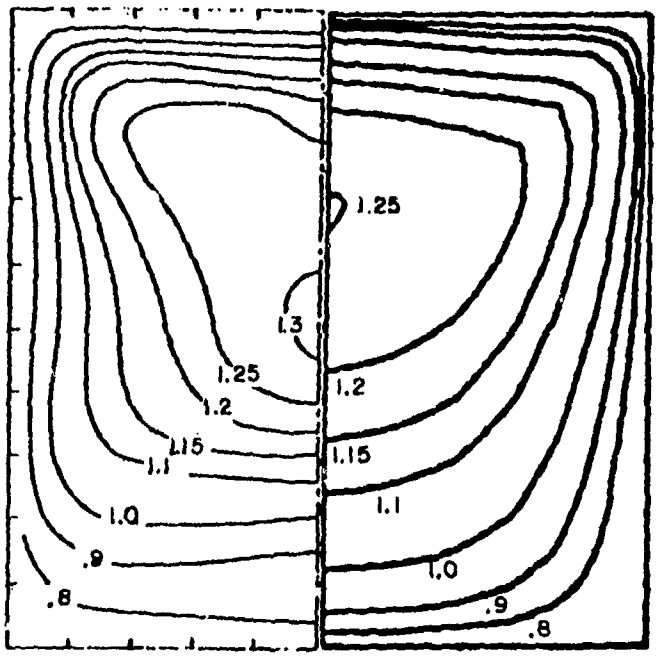

(C) 45°

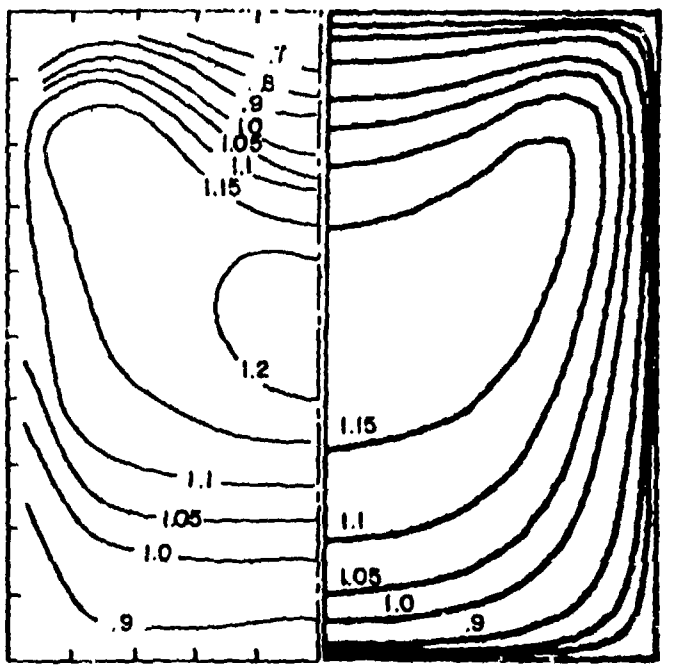

(D) 71°

Fig. 9 (Continued)

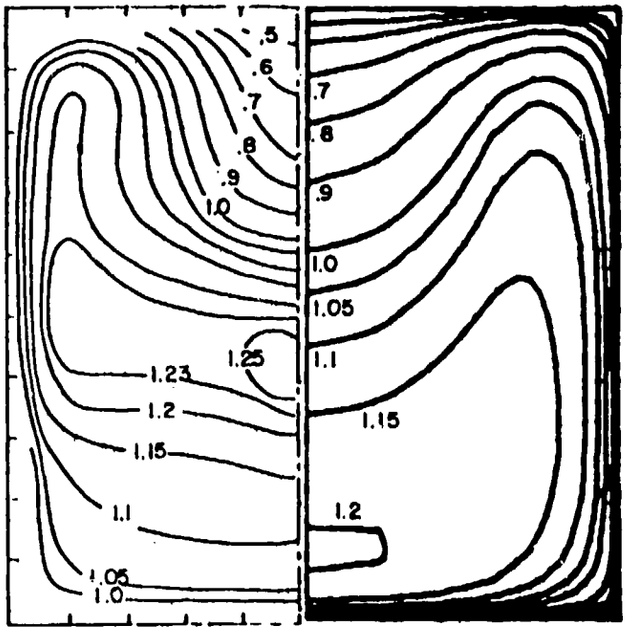

(E) 90°

Fig. 9 (Continued)

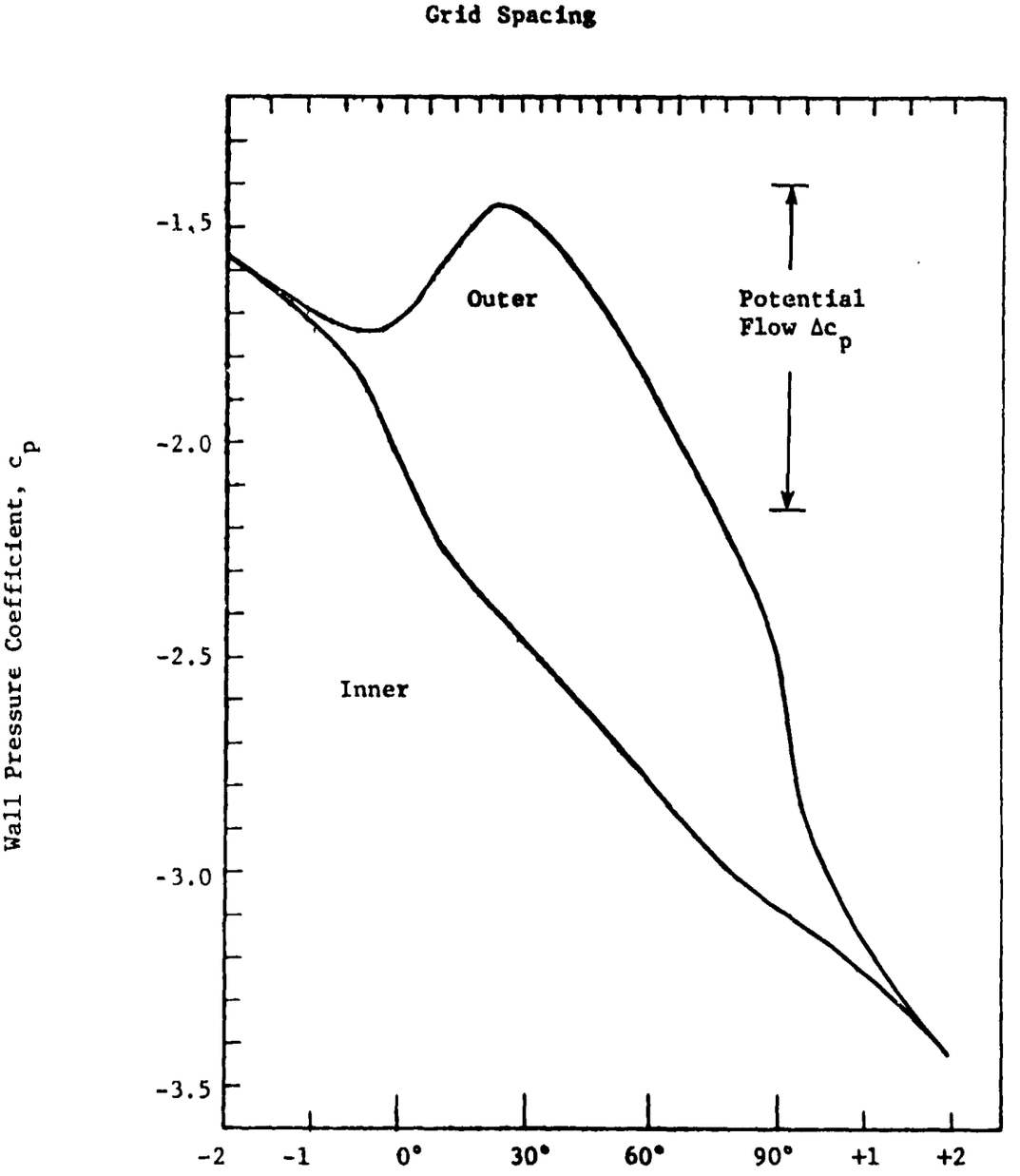

Fig. 10 - Laminar Pipe Bend (Case 1 - Re = 500, R/d = 2.8). Wall Pressure Coefficient in Centerline Plane of Symmetry.

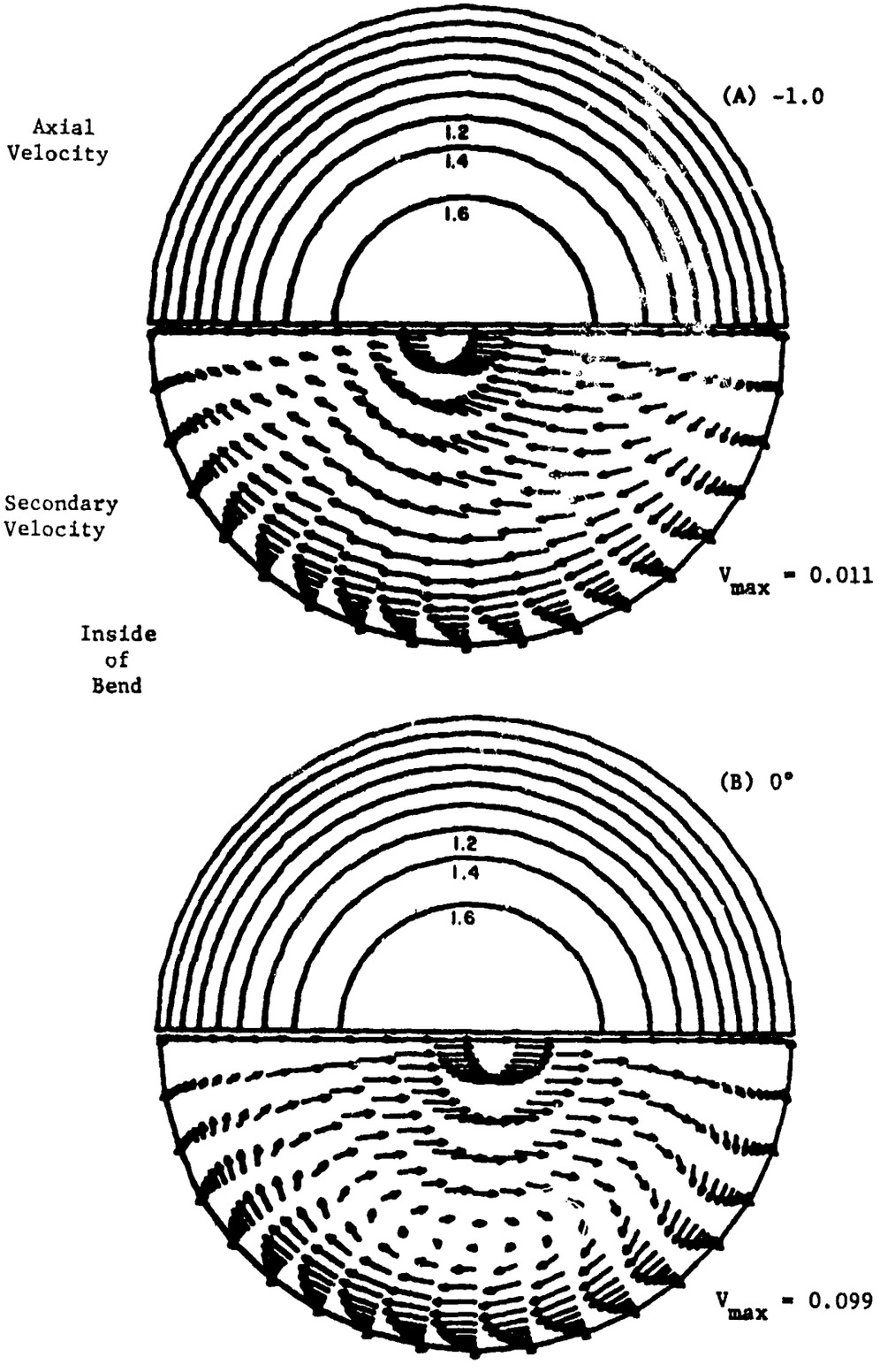

Fig. 11 - Laminar Pipe Bend (Case 1 - Re = 500, R/d = 2.8). Axial Development of Primary and Secondary Flow Structure.

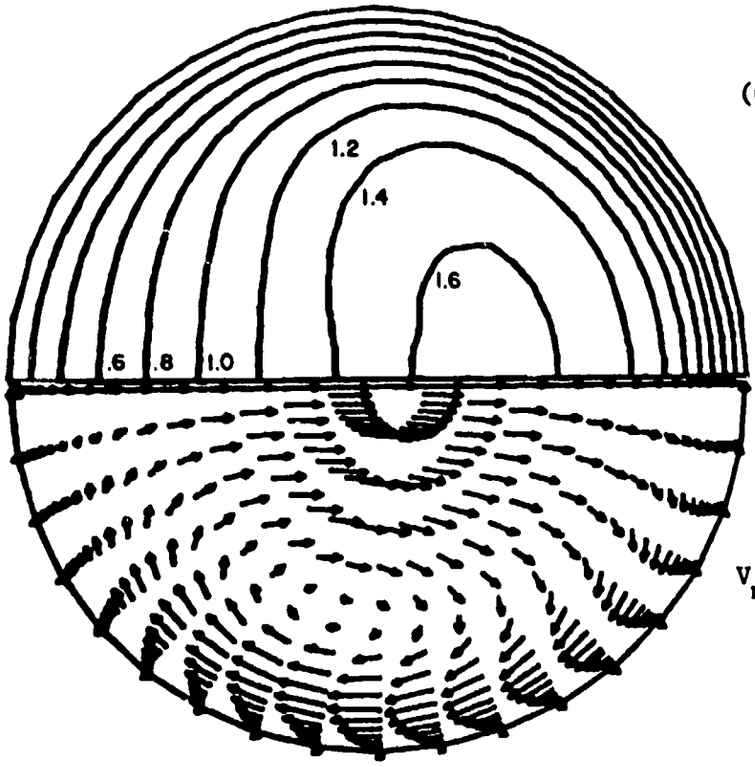

(C) 30°

V_{max} = 0.394

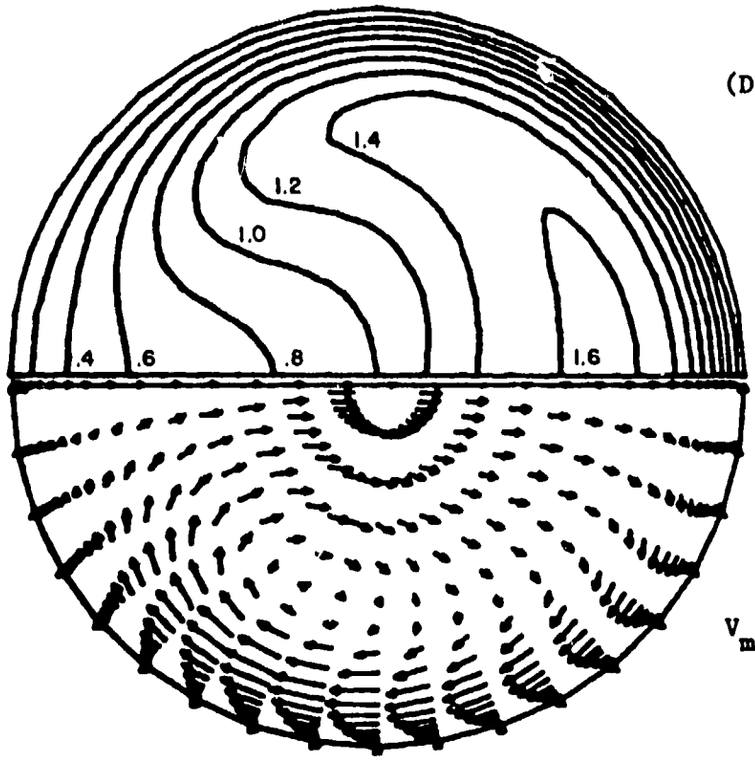

(D) 60°

V_{max} = 0.346

Fig. 11 (Continued)

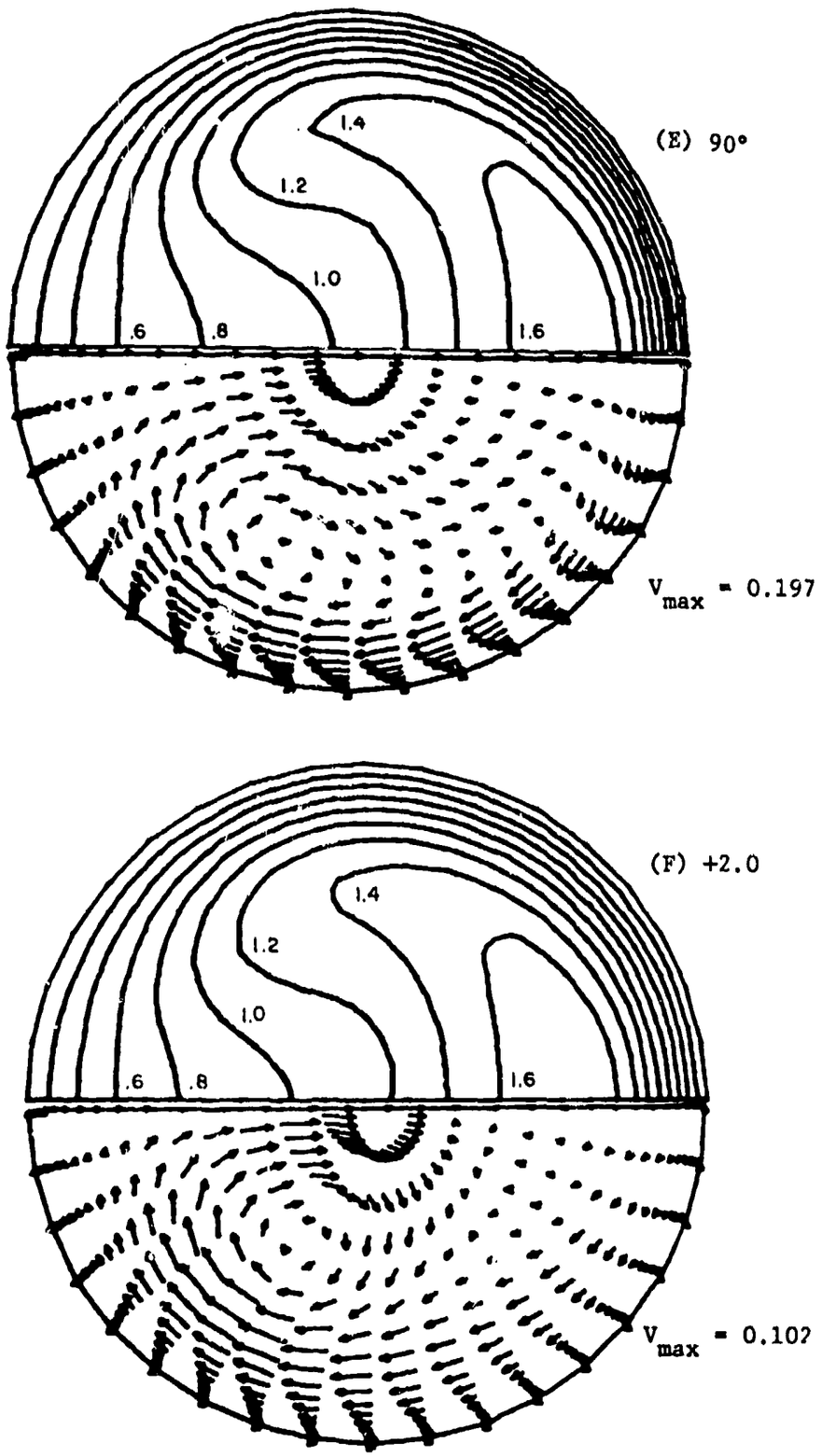

Fig. 11 (Continued)

Grid Spacing

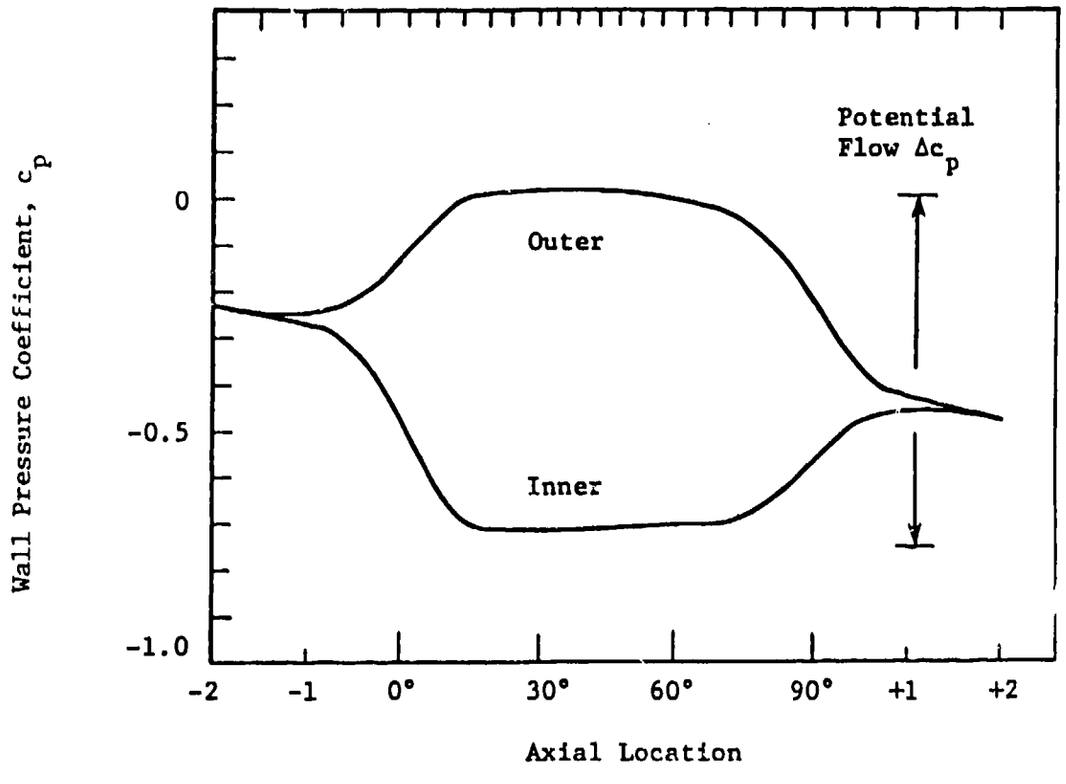

Fig. 12 - Turbulent Pipe Bend (Case 2 - Re = 43,000, R/d = 2.8). Wall Pressure Coefficient in Centerline Plane of Symmetry.

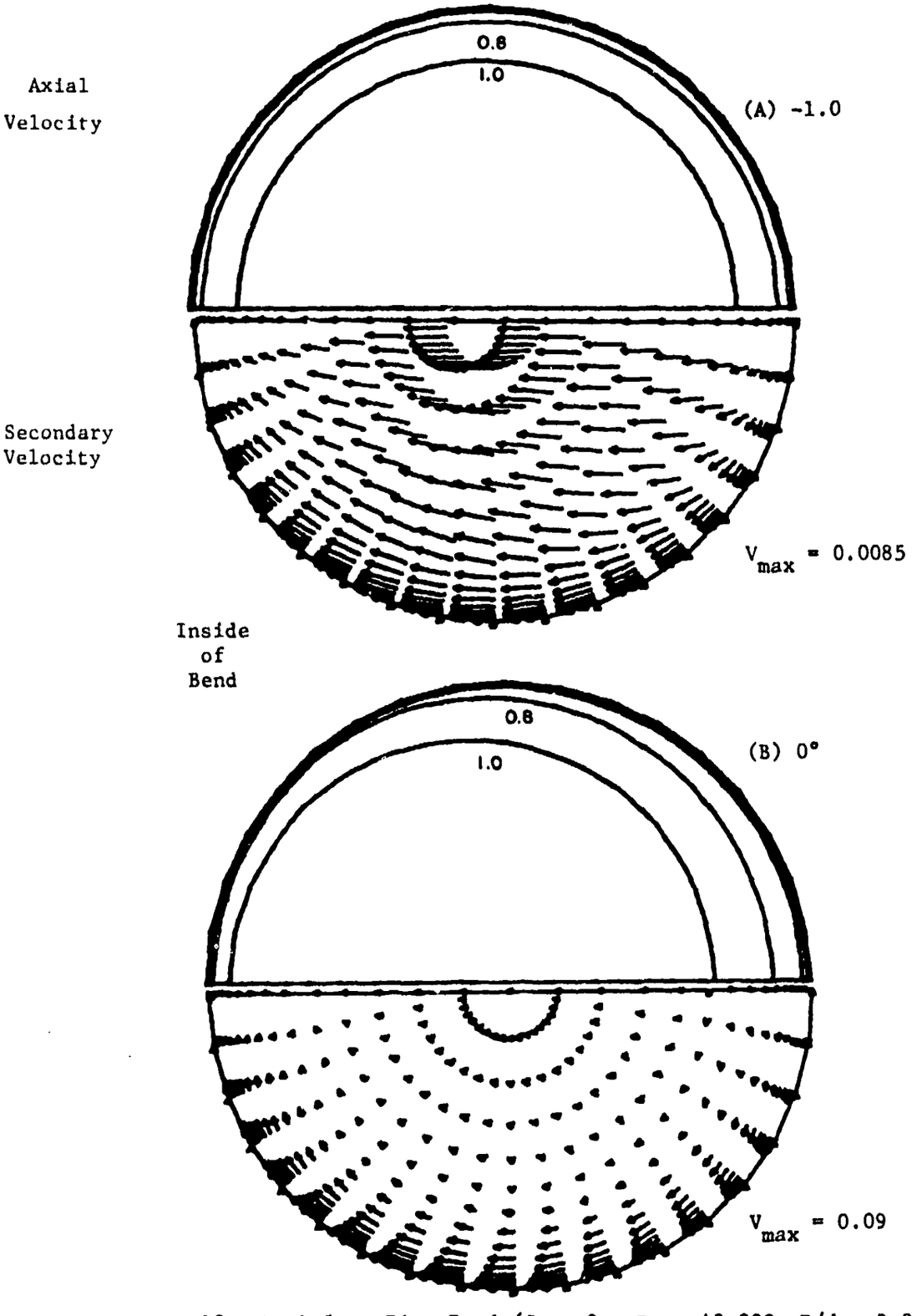

Fig. 13 - Turbulent Pipe Bend (Case 2 - Re = 43,000, R/d = 2.3).
Axial Development of Primary and Secondary Flow Structure.

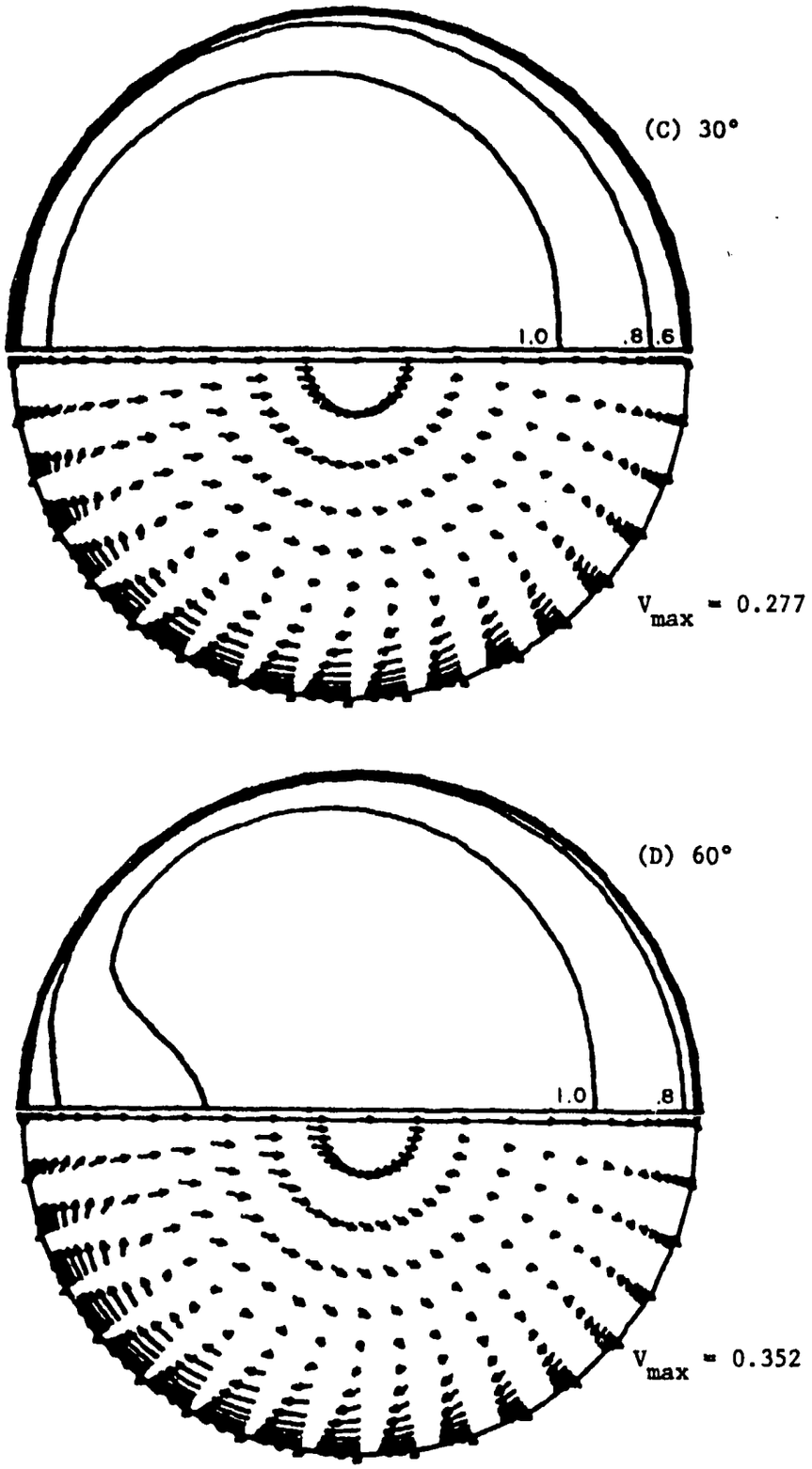

Fig. 13 (Continued)

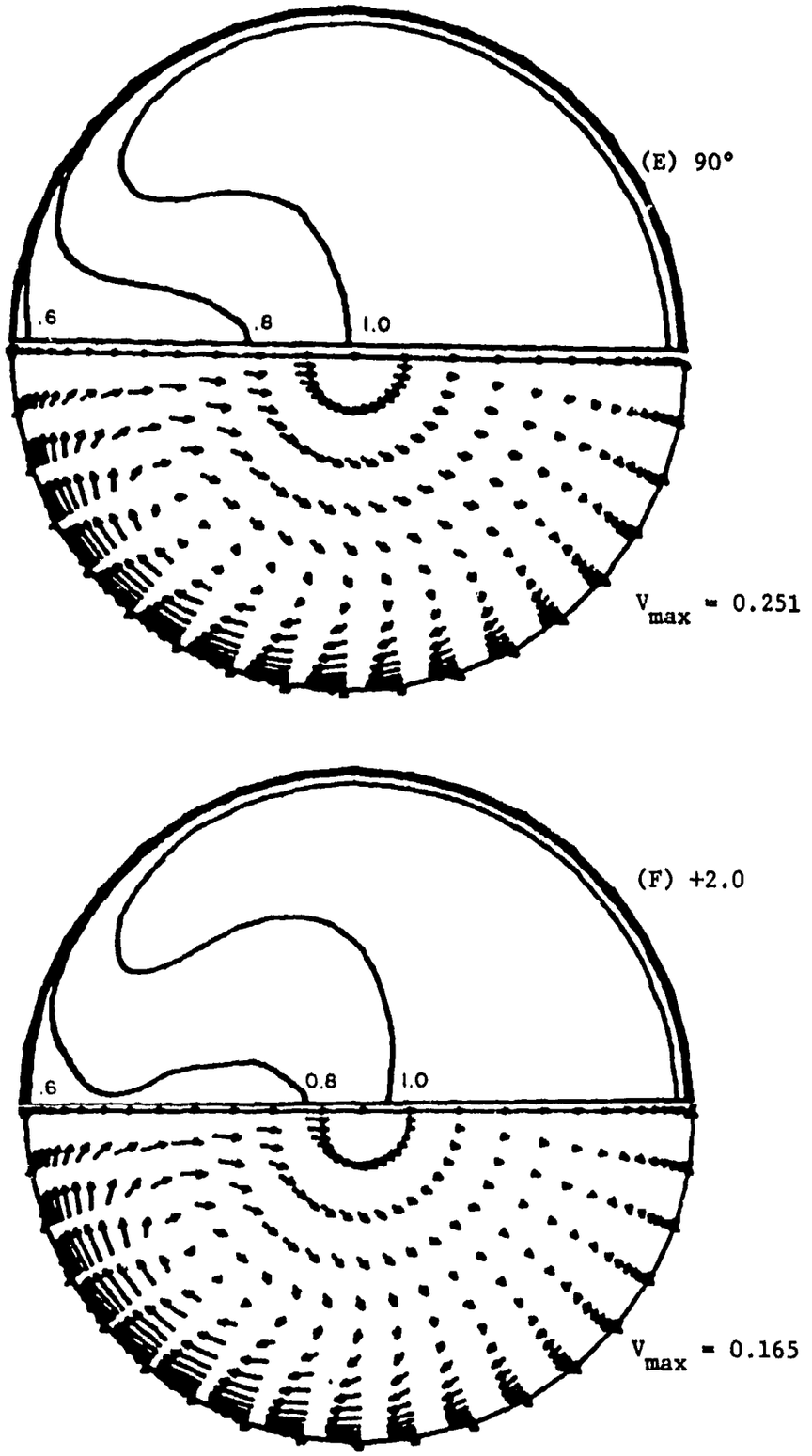

Fig. 13 (Continued)

Grid Spacing

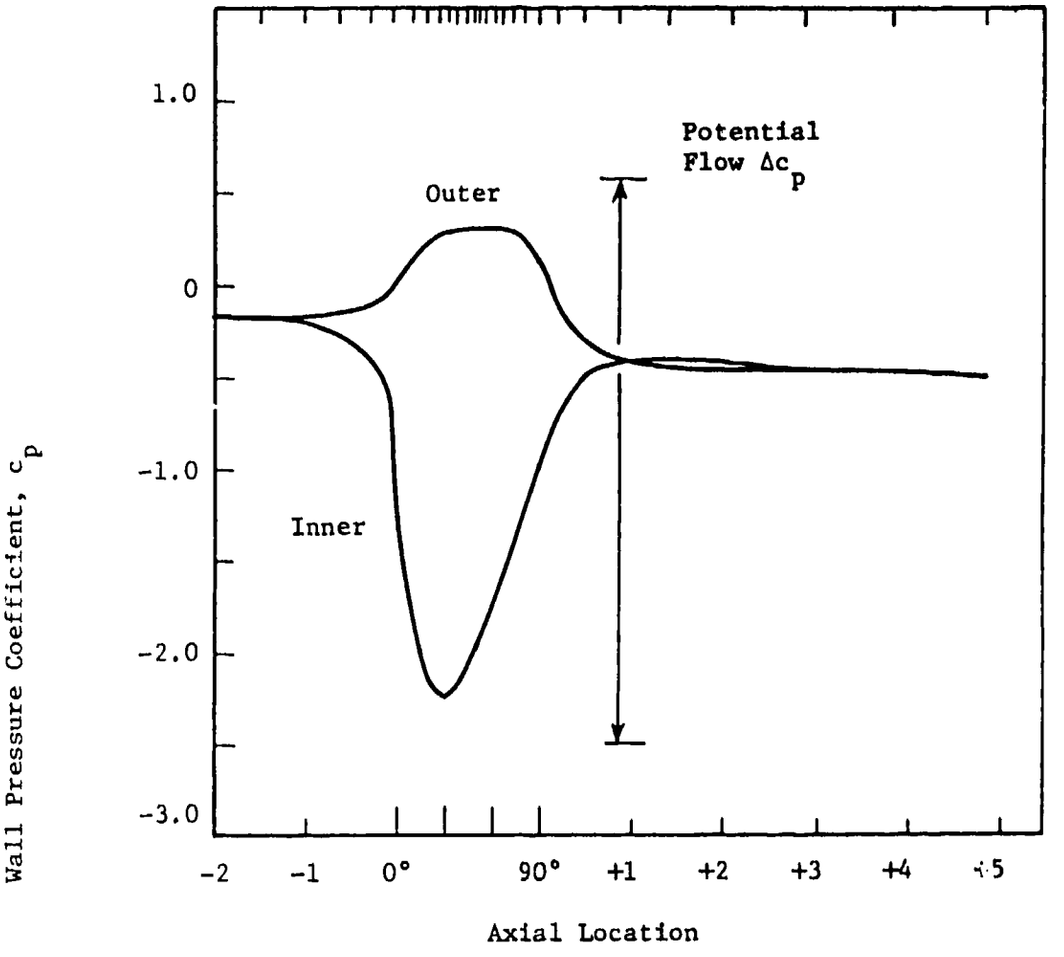

Fig. 14 - Turbulent Pipe Elbow (Case 3 - Re = 43,000, R/d = 1.0). Wall Pressure Coefficient in Centerline Plane of Symmetry.

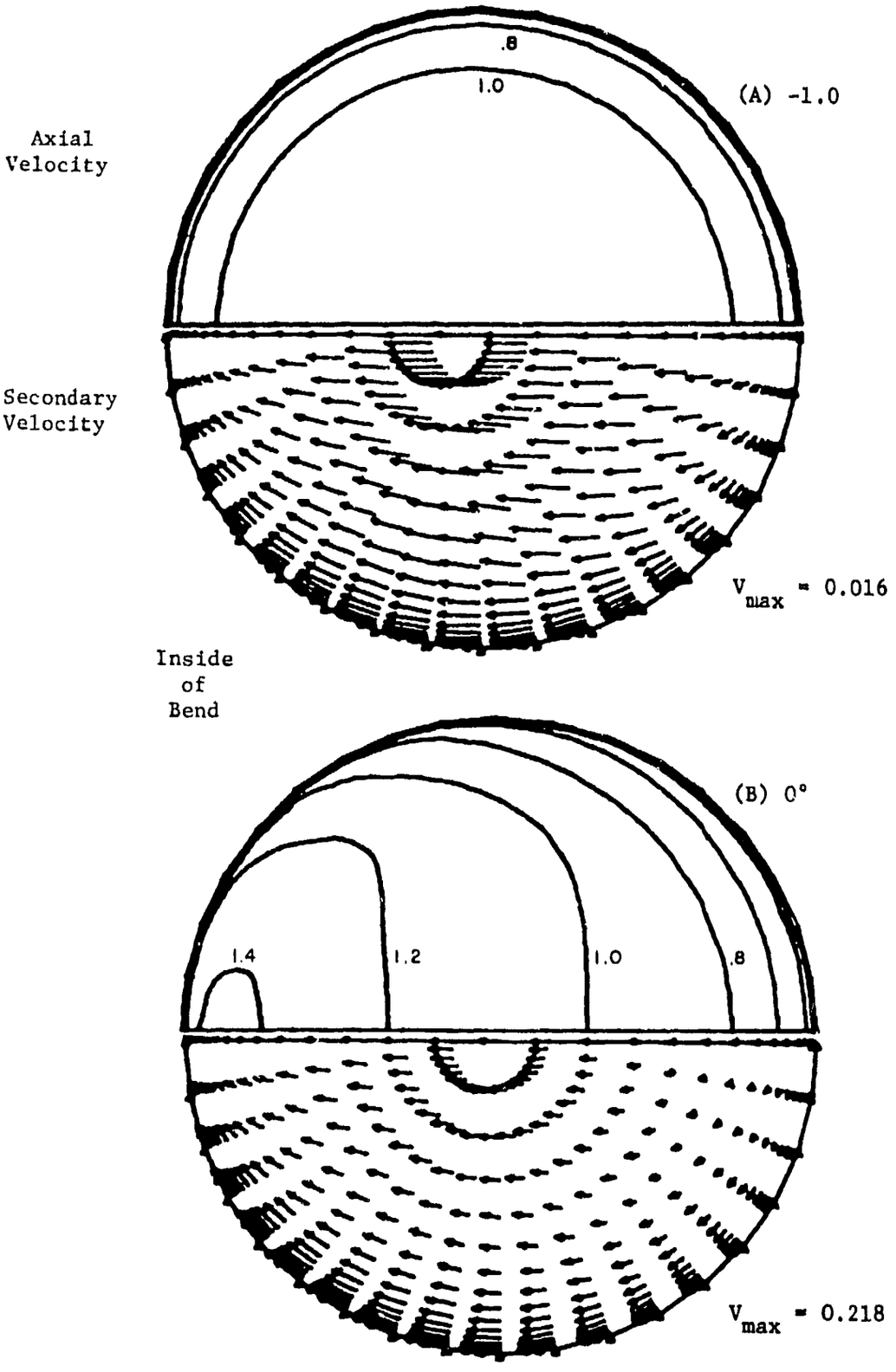

Fig. 15 - Turbulent Pipe Elbow (Case 3 - Re = 43,000, R/d = 1.0). Axial Development of Primary and Secondary Flow Structure.

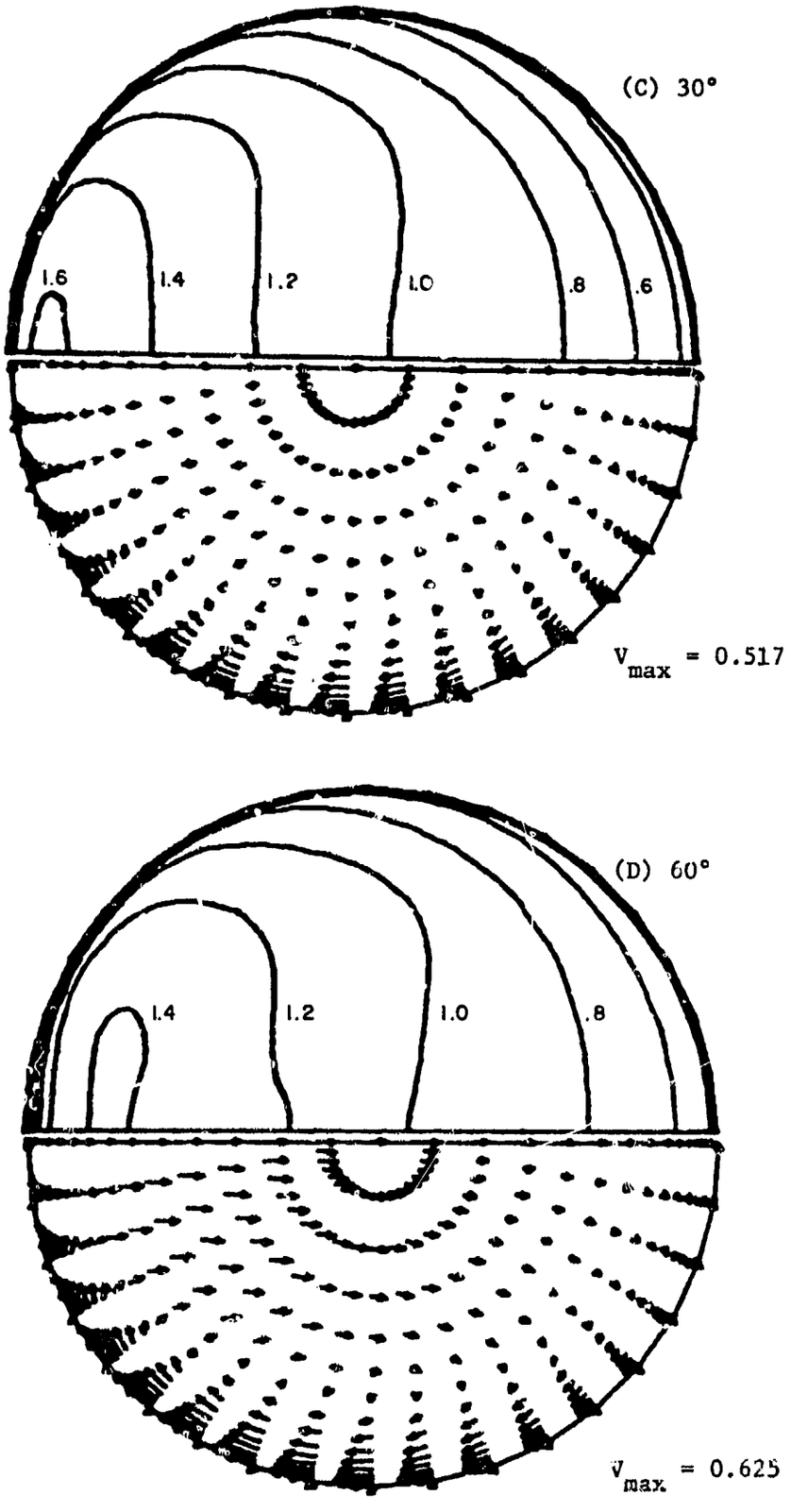

Fig. 15 (Continued)

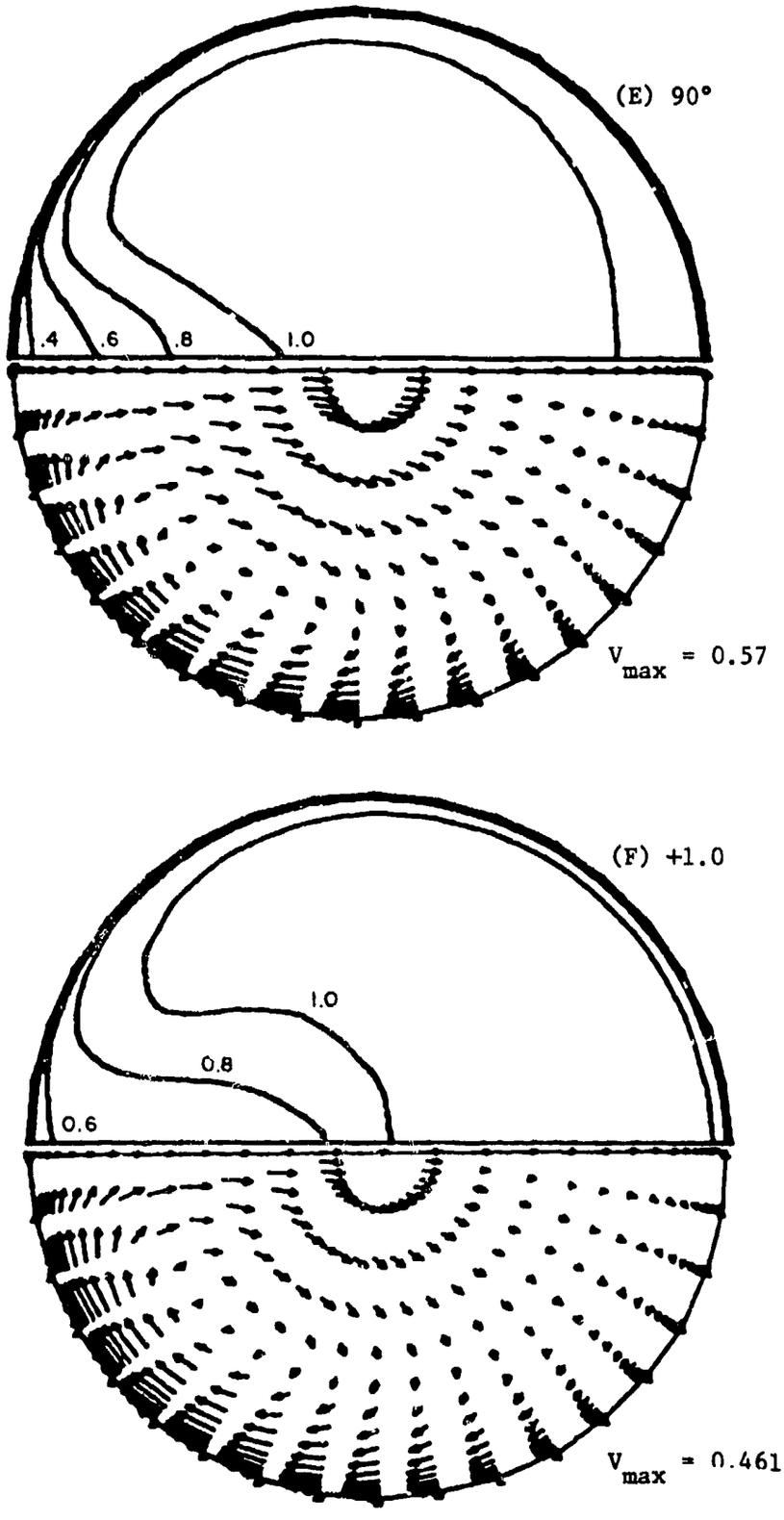

Fig. 15 (Continued)

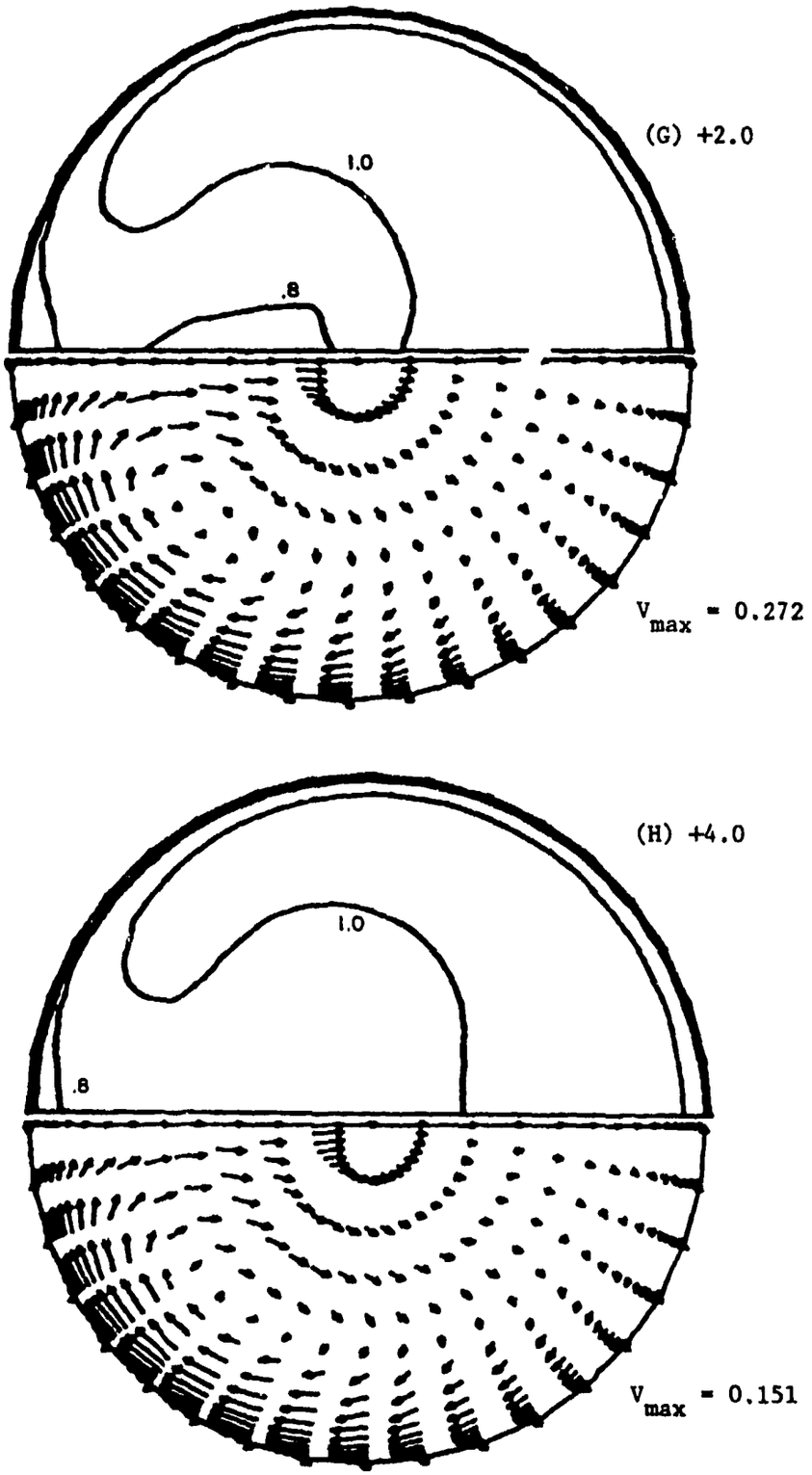

Fig. 15 (Continued)

(A) Axial Velocity at 60°

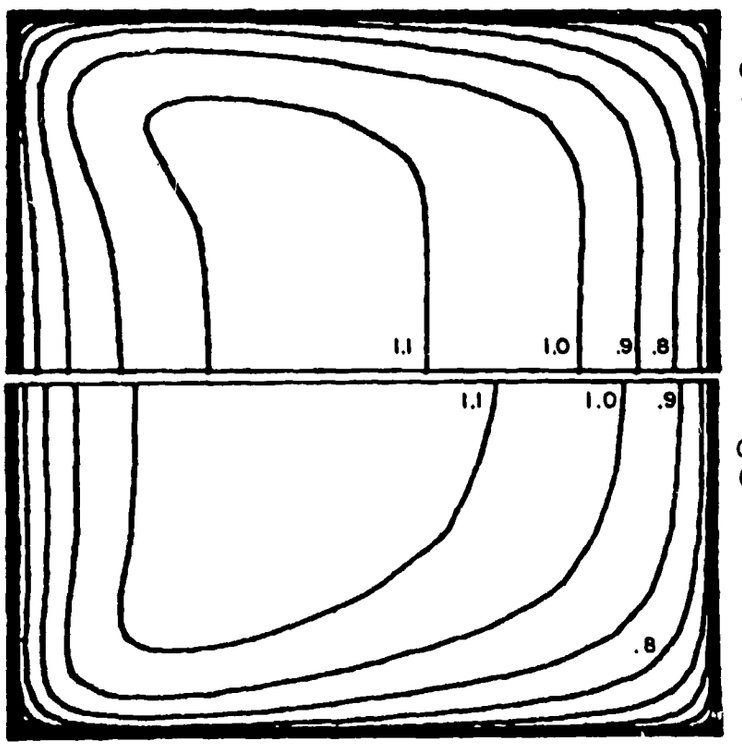

(B) Secondary Velocity

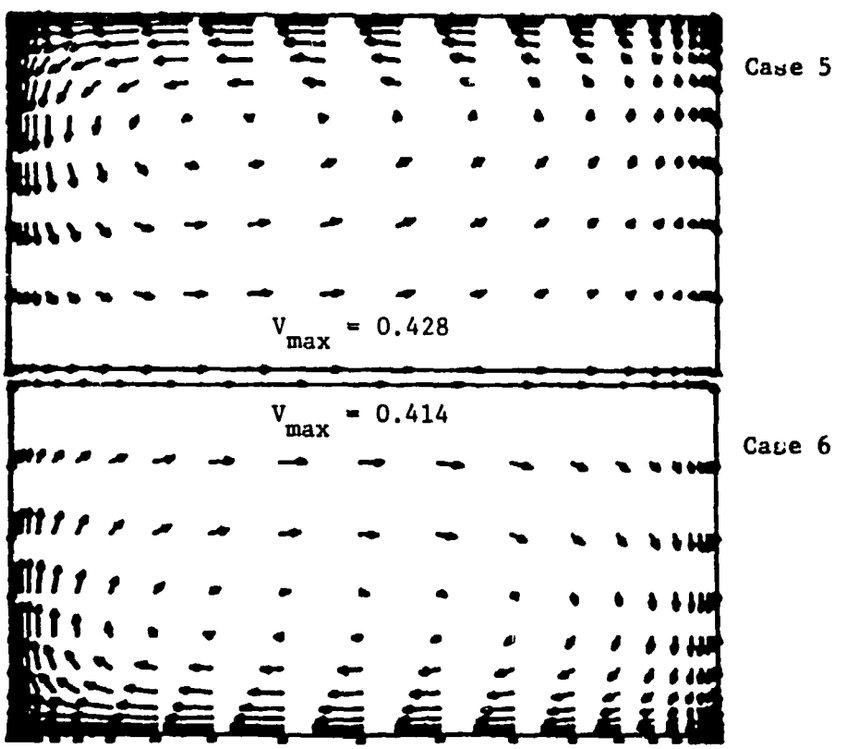

Fig. 16 - Flow Structure at 60 Degrees for Different Inflow Boundary Layer Thicknesses.

(A) Axial Velocity at 90°

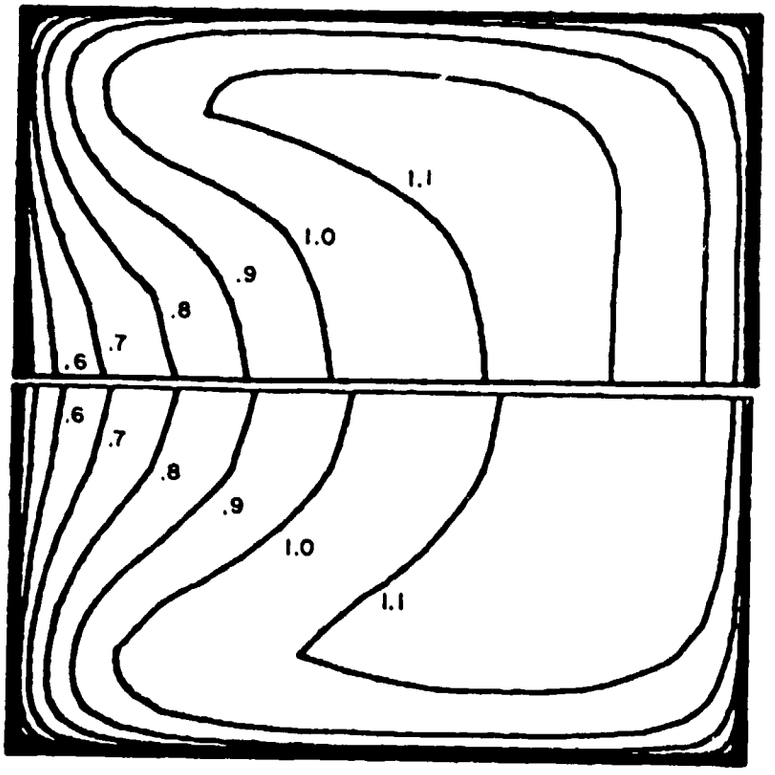

(B) Secondary Velocity

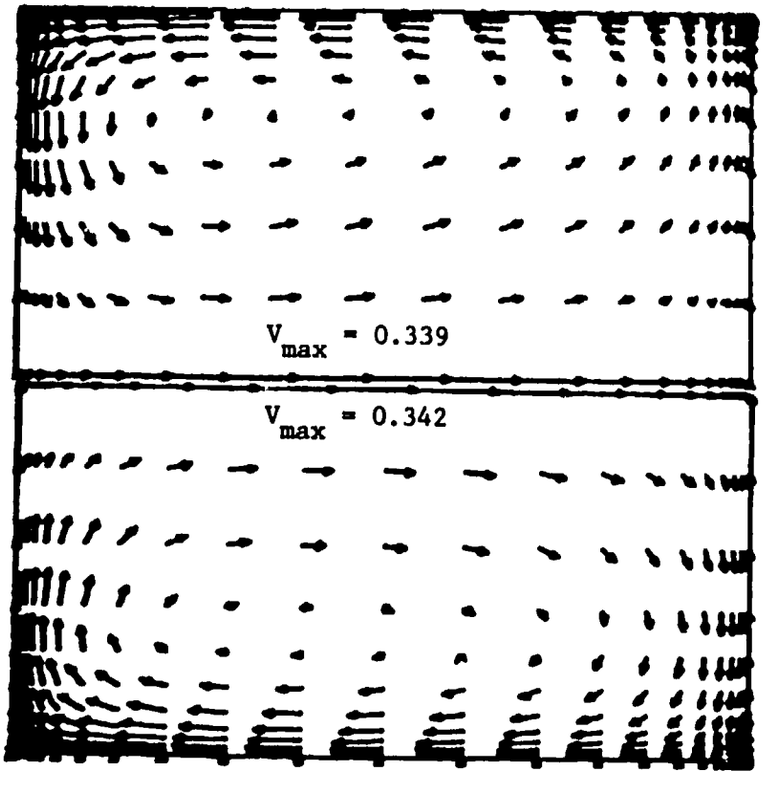

Fig. 17 - Flow Structure at 90 Degrees for Different Inflow Boundary Layer Thicknesses.

(A) Pressure Coefficient at 60°

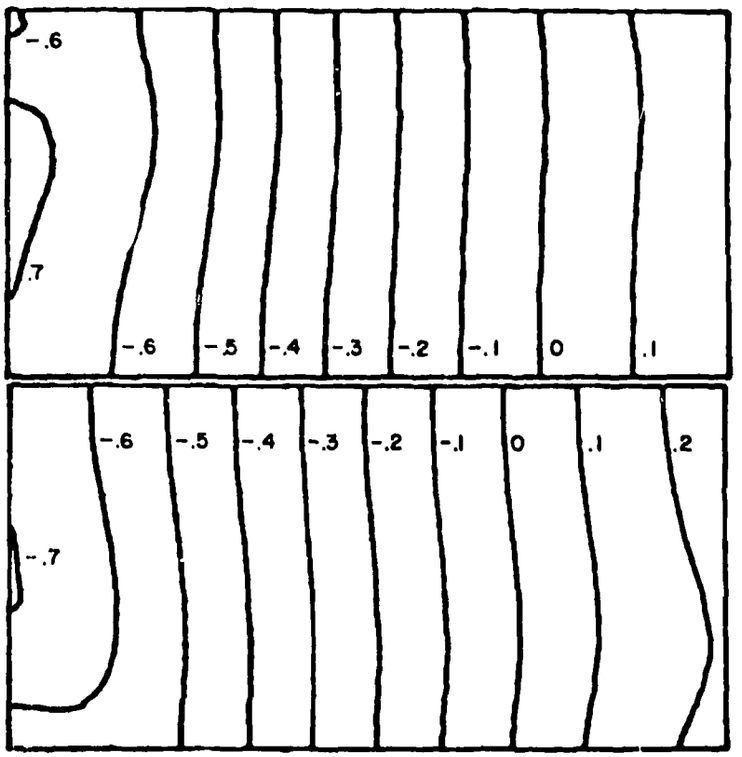

(B) Pressure Coefficient at 90°

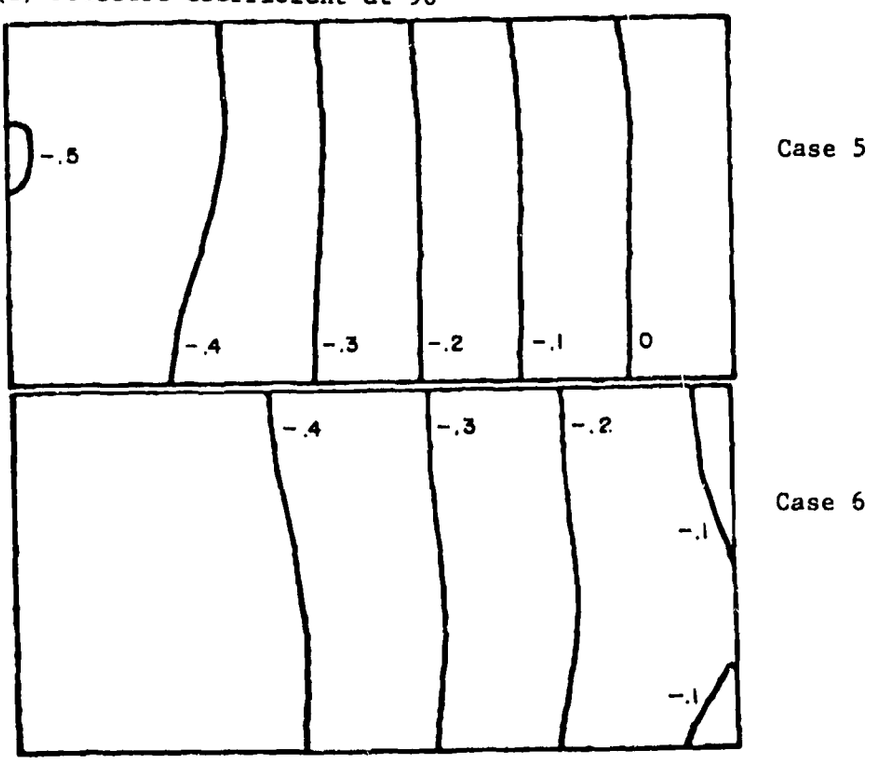

Fig. 18 - Pressure Coefficient for Different Inlet Boundary Layer Thicknesses.

DISTRIBUTION LIST (Continued)
Page Eight

Professor J.F. Thompson
Mississippi State University
Department of Aerophysics and
Aerospace Engineering
State College, MS 39762

AFDRD-AS/M
U.S. Air Force
The Pentagon
Washington, DC 20330

Air Force Office of Scientific
Research/NA
Building 410
Bolling AFB
Washington, DC 20332

Naval Air Systems Command
Code 03
Washington, DC 20361

Naval Air Systems Command
Code 03B
Washington, DC 20361

Naval Air Systems Command
Code 310
Washington, DC 20361

Mr. Raymond F. Siewert
Naval Air Systems Command
Code 320D
Washington, DC 20361

Naval Air Systems Command
Code 5301
Washington, DC 20361

Mr. Robert J. Hansen
Naval Research Laboratory
Code 8441
Washington, DC 20375

Mr. Walter Engle
Naval Sea Systems Command
Code 08
Washington, DC 20362

Dr. S. Beus
Bettis Atomic Power Laboratory
P.O. Box 79
West Mifflin, PA 15122

Mr. M. Lubert
General Electric Company
Knolls Atomic Power Laboratory
P.O. Box 1072
Schnectady, NY 12301

Professor Ronald W. Yeung
Massachusetts Institute of Technology
Department of Ocean Engineering
Cambridge, MA 02139

Professor Allen Plotkin
University of Maryland
Department of Aerospace Engineering
College Park, MD 20742

Professor J.M. Burgers
University of Maryland
Institute of Fluid Dynamics
and Applied Mathematics
College Park, MD 20742

Dr. Robert K.-C. Chan
JAYCOR
1401 Camino Del Mar
Del Mar, CA 92014

Dr. Robert H. Kraichnan
Dublin, NH 03444

Mr. Dennis Bushnell
NASA-Langley Research Center
Langley Station
Hampton, VA 23365

Technical Library
Naval Ordnance Station
Indian Head, MD 20640

Professor S.F. Shen
Cornell University
Sibley School of Mechanical
and Aerospace Engineering
Ithaca, NY 14853

Mr. Marshall P. Tulin
Hydronautics, Incorporated
7210 Pindell School
Laurel, MD 20810

Dr. J.C.W. Rogers
The Johns Hopkins University
Applied Physics Laboratory
Johns Hopkins Road
Laurel, MD 20810

Mr. John L. Hess
Douglas Aircraft Company
3855 Lakewood Boulevard
Long Beach, CA 90801

Dr. H.K. Cheng
University of Southern California
University Park
Department of Aerospace Engineering
Los Angeles, CA 90007

Professor J.J. Stoker
New York University
Courant Institute of
Mathematical Sciences
251 Mercer Street
New York, NY 10003

Librarian, Aeronautical Laboratory
National Research Council
Montreal Road
Ottawa 7, Canada

Professor Norman J. Zabusky
University of Pittsburgh
Department of Mathematics
and Statistics
Pittsburgh, PA 15260

Technical Library
Naval Missile Center
Point Mugu, CA 93041

Dr. Harvey Segur
Aeronautical Research Associates
of Princeton, Inc.
50 Washington Road
Princeton, NJ 08540

Professor S.I. Cheng
Princeton University
Department of Aerospace and
Mechanical Sciences
The Engineering Quadrangle
Princeton, NJ 08540

Dr. T.F. Zien
Naval Surface Weapons Center
White Oak Laboratory
Room 427-544
Silver Spring, MD 20910

Dr. Gary Chapman
Ames Research Center
Mail Stop 227-4
Moffett Field, CA 94035

Deputy Director
Tactical Technology Office
Defense Advanced Research
Projects Agency
1400 Wilson Boulevard
Arlington, VA 22209

Professor Alexandre J. Chorin
University of California
Center for Pure and Applied Mathematics
Berkeley, CA 94720

Professor Joseph L. Hammack, Jr.
University of California
Department of Civil Engineering
Berkeley, CA 94720

Professor Paul Lieber
University of California
Department of Mechanical Engineering
Berkeley, CA 94720

Dr. Harvey R. Chaplin, Jr.
David W. Taylor Naval Ship Research
and Development Center
Code 1600
Bethesda, MD 20084

Dr. Francois N. Frenkiel
David W. Taylor Naval Ship Research
and Development Center
Code 1802.2
Bethesda, MD 20084

Mr. Gene H. Gleissner
David W. Taylor Naval Ship Research
and Development Center
Code 1800
Bethesda, MD 20084

Dr. Pao C. Pien
David W. Taylor Naval Ship Research
and Development Center
Code 1521
Bethesda, MD 20084

Dr. Nils Salvesen
David W. Taylor Naval Ship Research
and Development Center
Code 1552
Bethesda, MD 20084

Mrs. Joanna W. Schot
David W. Taylor Naval Ship Research
and Development Center
Code 1843
Bethesda, MD 20084

Dr. George R. Inger
Virginia Polytechnic Institute
and State University
Department of Aerospace and
Ocean Engineering
Blacksburg, VA 24061

Dr. Ali H. Nayfeh
Virginia Polytechnic Institute
and State University
Department of Engineering Mechanics
Blacksburg, VA 24061

Professor C. C. Mei
Massachusetts Institute of Technology
Department of Civil Engineering
Cambridge, MA 02139

Professor David J. Benney
Massachusetts Institute of Technology
Department of Mathematics
Cambridge, MA 02139

Professor Phillip Mandel
Massachusetts Insitute of Technology
Department of Ocean Engineering
Cambridge, MA 02139

Professor J. Nicholas Newman
Massachusetts Institute of Technology
Department of Ocean Engineering
Room 5-324A
Cambridge, MA 02139

Professor Francis Noblesse
Masachusetts Institute of Technology
Department of Ocean Engineering
Cambridge, MA 02139

Professor L. Gary Leal
California Insitute of Technology
Division of Chemistry and Chemical Engineering
Pasadena, CA 91125

Professor H.W. Liepmann
California Insitute of Technology
Graduate Aeronautical Laboratories
Pasadena, CA 91125

Professor A. Roshko
California Institute of Technology
Graduate Aeronautical Laboratories
Pasadena, CA 91125

Dr. Leslie M. Mack
Jet Propulsion Laboratory
California Institute of Technology
Pasadena, CA 91103

Professor K.M. Agrawal
Virginia State College
Department of Mathematics
Petersburg, VA 23803

Technical Library
Naval Missile Center
Point Mugu, CA 93041

Professor Francis R. Hama
Princeton University
Department of Mechanical and
Aerospace Engineering
Princeton, NJ 08540

Dr. Joseph H. Clarke
Brown University
Division of Engineering
Providence, RI 02912

Professor J.T.C. Liu
Brown University
Division of Engineering
Providence, RI 02912

Chief, Document Section
Redstone Scientific Information Center
Army Missile Command
Redstone Arsenal, AL 35809

Dr. Jack W. Hoyt
Naval Ocean Systems Center
Code 2591
San Diego, CA 92152

Professor Richard L. Pfeffer
Florida State University
Geophysical Fluid Dynamics Institute
Tallahassee, FL 32306

Dr. Denny R.S. Ko
Dynamics Technology, Inc.
22939 Hawthorne Boulevard, Suite 200
Torrance, CA 90505

Professor Thomas J. Hanratty
University of Illinois at
Urbana-Champaign
Department of Chemical Engineering
205 Roger Adams Laboratory
Urbana, IL 61801

Air Force Office of Scientific
Research/NA
Building 410
Bolling AFB
Washington, DC 20332

Professor Hsien-Ping Pao
The Catholic University of America
Department of Civil Engineering
Washington, DC 20064

Dr. Phillip S. Klebanoff
National Bureau of Standards
Mechanics Section
Washington, DC 20234

Dr. G. Kulin
National Bureau of Standards
Mechanics Section
Washington, DC 20234

Dr. J.O. Elliot
Naval Research Laboratory
Code 8310
Washington, DC 20375

Mr. R.J. Hansen
Naval Research Laboratory
Code 8441
Washington, DC 20375

Professor S.I. Pai
University of Maryland
Institute of Fluid Dynamics
and Applied Mathematics
College Park, MD 20742

Computation and Analyses Laboratory
Naval Surface Weapons Center
Dahlgren Laboratory
Dahlgren, VA 22418

Dr. Robert H. Kraichnan
Dublin, NH 03444

Professor Robert E. Falco
Michigan State University
Department of Mechanical Engineering
East Lansing, MI 48824

Professor E. Rune Lindgren
University of Florida
Department of Engineering Sciences
231 Aerospace Engineering Building
Gainesville, FL 32611

Mr. Dennis Bushnell
NASA Langley Research Center
Langely Station
Hampton, VA 23365

Dr. A.K.M. Fazle Hussain
University of Houston
Department of Mechanical Engineering
Houston, TX 77004

Professor John L. Lumley
Cornell University
Sibley School of Mechanical
and Aerospace Engineering
Ithaca, NY 14853

Professor K.E. Shuler
University of California, San Diego
Department of Chemistry
La Jolla, CA 92093

Dr. E.W. Montroll
Physical Dynamics, Inc.
P.O. Box 556
La Jolla, CA 92038

Mr. Steven A. Orszag
Cambridge Hydrodynamics, Inc.
54 Baskin Road
Lexington, MA 02173

Professor Tuncer Cebeci
California State University
Mechanical Engineering Department
Long Beach, CA 90840

Dr. C.W. Hirt
University of California
Los Alamos Scientific Laboratory
P.O. Box 1663
Los Alamos, NM 87544

Professor Frederick K. Browand
University of Southern California
University Park
Department of Aerospace Engineering
Los Angeles, CA 90007

Professor John Laufer
University of Southern California
University Park
Department of Aerospace Engineering
Los Angeles, CA 90007

Professor T.R. Thomas
Teesside Polytechnic
Department of Mechanical Engineering
Middlesbrough TS1 3BA, ENGLAND

Dr. Arthur B. Metzner
University of Delaware
Department of Chemical Engineering
Newark, DE 19711

Professor Harry E. Rauch
The Graduate School and University
Center of the City University
of New York
Graduate Center: 33 West 42 Street
New York, NY 10036

Mr. Norman M. Nilsen
Dyntec Company
5301 Laurel Canyon Blvd., Suite 201
North Hollywood, CA 91607

Librarian Station 5-2
Coast Guard Headquarters
NASSIF Building
400 Seventh Street, SW
Washington, DC 20591

Library of Congress
Science and Technology Division
Washington, DC 20540

Dr. A.L. Slafkosky
Scientific Advisor
Commandant of the Marine Corps
Code AX
Washington, DC 20380

Maritime Administration
Office of Maritime Technology
14th & E Streets, NW
Washington, DC 20230

Maritime Administration
Division of Naval Architecture
14th & E Streets, NW
Washington, DC 20230

Dr. G. Kulin
National Bureau of Standards
Mechanics Section
Washington, DC 20234

Naval Research Laboratory
Code 2627
Washington, DC 20375 6 copies

Library
Naval Sea Systems Command
Code 09GS
Washington, DC 20362

Mr. Thomas E. Peirce
Naval Sea Systems Command
Code 03512
Washington, DC 20362

Mr. Stanley W. Doroff
Mechanical Technology, Inc.
2731 Prosperity Avenue
Fairfax, VA 22031

Dr. Charles Watkins, Head
Mechanical Engineering Department
Howard University
Washington, DC 20059

Professor W.W. Willmarth
The University of Michigan
Department of Aerospace Engineering
Ann Arbor, MI 48109

Office of Naval Research
Code 481
800 N. Quincy Street
Arlington, VA 22217

Professor Richard W. Miksad
The University of Texas at Austin
Department of Civil Engineering
Austin, TX 78712

Professor Stanley Corrsin
The Johns Hopkins University
Department of Mechanics and
Materials Sciences
Baltimore, MD 21218

Professor Paul Lieber
University of California
Department of Mechanical Engineering
Berkeley, CA 94720

Professor P.S. Virk
Massachusetts Institute of Technology
Department of Chemical Engineering
Cambridge, MA 02139

Professor E. Mollo-Christensen
Massachusetts Institute of Technology
Department of Meteorology
Room 54-1722
Cambridge, MA 02139

Professor Patrick Leehey
Massachusetts Institute of Technology
Department of Ocean Engineering
Cambridge, MA 02139

Professor Eli Reshotko
Case Western Reserve University
Department of Mechanical and
Aerospace Engineering
Cleveland, OH 44106

DISTRIBUTION LIST (Continued)
Page Two

Library
Naval Weapons Center
China Lake, CA 93555

Technical Library
Naval Surface Weapons Center
Dahlgren Laboratory
Dahlgren, VA 22418

Technical Documents Center
Army Mobility Equipment Research Center
Building 315
Fort Belvoir, VA 22060

Technical Library
Webb Institute of Naval Architecture
Glen Cove, NY 11542

Dr. J.P. Breslin
Stevens Institute of Technology
Davidson Laboratory
Castle Point Station
Hoboken, NJ 07030

Professor Louis Landweber
The University of Iowa
Institute of Hydraulic Research
Iowa City, IA 52242

R.E. Gibson Library
The Johns Hopkins University
Applied Physics Laboratory
Johns Hopkins Road
Laurel, MD 20810

Lorenz G. Straub Library
University of Minnesota
St. Anthony Falls Hydraulic Laboratory
Minneapolis, MN 55414

Library
Naval Postgraduate School
Monterey, CA 93940

Technical Library
Naval Underwater Systems Center
Newport, RI 02840

Engineering Societies Library
345 East 47th Street
New York, NY 10017

The Society of Naval Architects and
Marine Engineers
One World Trade Center, Suite 1369
New York, NY 10048

Technical Library
Naval Coastal System Laboratory
Panama City, FL 32401

Professor Theodore Y. Wu
California Insitute of Technology
Engineering Science Department
Pasadena, CA 91125

Director
Office of Naval Research Western
Regional Office
1030 E. Green Street
Pasadena, CA 91101

Technical Library
Naval Ship Engineering Center
Philadelphia Division
Philadelphia, PA 19112

Army Research Office
P.O. Box 12211
Research Triangle Park, NC 27709

Editor
Applied Mechanics Review
Southwest Research Institute
8500 Culebra Road
San Antonio, TX 78206

Technical Library
Naval Ocean Systems Center
San Diego, CA 92152

ONR Scientific Liaison Group
American Embassy - Room A-407
APO San Francisco 96503

Librarian
Naval Surface Weapons Center
White Oak Laboratory
Silver Spring, MD 20910

Defense Research and Development Attache
Australian Embassy
1601 Massachusetts Avenue, NW
Washington, DC 20036

DISTRIBUTION LIST FOR UNCLASSIFIED
TECHNICAL REPORTS AND REPRINTS ISSUED UNDER
CONTRACT N00014-81-C-0377 TASK 062-648

All addressees receive one copy unless otherwise specified

Defense Technical Information Center
Cameron Station
Alexandria, VA 22314 12 copies

Professor Bruce Johnson
U.S. Naval Academy
Engineering Department
Annapolis, MD 21402

Library
U.S. Naval Academy
Annapolis, MD 21402

Technical Library
David W. Taylor Naval Ship Research
and Development Center
Annapolis Laboratory
Annapolis, MD 21402

Professor C.-S. Yih
The University of Michigan
Department of Engineering Mechanics
Ann Arbor, MI 48109

Professor T. Francis Ogilvie
The University of Michigan
Department of Naval Architecture
and Marine Engineering
Ann Arbor, MI 48109

Office of Naval Research
Code 200B
800 N. Quincy Street
Arlington, VA 22217 3 copies

Office of Naval Research
Code 438
800 N. Quincy Street
Arlington, VA 22217

Office of Naval Research
Code 473
800 N. Quincy Street
Arlington, VA 22217

NASA Scientific and Technical
Information Facility
P.O. Box 8757
Baltimore/Washington
International Airport
Maryland, 21240

Professor Paul M. Naghdi
University of California
Department of Mechanical Engineering
Berkeley, CA 94720

Librarian
University of California
Department of Naval Architecture
Berkeley, CA 94720

Professor John V. Wehausen
University of California
Department of Naval Architecture
Berkeley, CA 94720

Library
David W. Taylor Naval Ship Research
and Development Center
Code 522.1
Bethesda, MD 20084

Mr. Justin H. McCarthy, Jr.
David W. Taylor Naval Ship Research
and Development Center
Code 1552
Bethesda, MD 20084

Dr. William B. Morgan
David W. Taylor Naval Ship Research
and Development Center
Code 1540
Bethesda, MD 20084

Director
Office of Naval Research Eastern/Central
Building 114, Section D - Regional Office
666 Summer Street
Boston, MA 02210